GPO 2/16/68

K fm #

00004

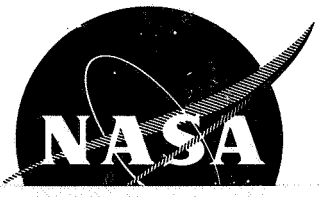

DISCHARGE CHAMBER STUDIES FOR MERCURY BOMBARDMENT ION THUSTERS

CONTRACT NO. NAS 3-9703

prepared by

W. KNAUER AND R. POESCHEL

for

NATIONAL AERONAUTICS AND SPACE ADMINISTRATION
LEWIS RESEARCH CENTER
CLEVELAND, OHIO

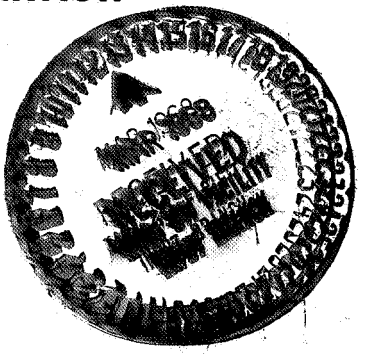

HUGHES

HUGHES AIRCRAFT COMPANY

RESEARCH LABORATORIES

3011 MALIBU CANYON ROAD
MALIBU, CALIFORNIA 90265

NASA-CR-72350

SEMIANNUAL REPORT

DISCHARGE CHAMBER STUDIES FOR MERCURY BOMBARDMENT ION THRUSTERS

by

W. Knauer and R. Poeschel

Prepared for

NATIONAL AERONAUTICS AND SPACE ADMINISTRATION
LEWIS RESEARCH CENTER
CLEVELAND, OHIO

CONTRACT NAS 3-9703

HUGHES RESEARCH LABORATORIES
a division of hughes aircraft company
3011 Malibu Canyon Road
Malibu, California

TABLE OF CONTENTS

LIST OF ILLUSTRATIONS v

I. INTRODUCTION 1

II. DISCHARGE DIAGNOSTIC EXPERIMENTS 3

A. Description of Experimental Thruster 3

B. Magnetic Field Variations and Thruster Performance 5

C. Analysis of Langmuir Probe Measurements 11

D. Langmuir Probe Measurements in the Thruster Discharge 18

III. OPTIMIZATION 25

IV. DISCHARGE THEORY 43

V. SUMMARY 47

REFERENCES 49

APPENDIX — Discharge Theory 51

LIST OF ILLUSTRATIONS

Fig. 1. Schematic drawing of the versatile experimental thruster used in diagnostic and optimization experiments 4

Fig. 2. Pictorial drawing showing dimensions of the Langmuir probe used in the experiments described in this report 4

Fig. 3. Photograph of powdered iron field map of magnetic field configuration in a thruster discharge chamber 6

Fig. 4. Magnetic field configuration generated in ET I by the coil currents shown, referred to as MF 4 7

Fig. 5. Magnetic field configuration generated in ET I by the coil currents shown, referred to as MF 5. 8

Fig. 6. Magnetic field configuration generated in ET I by the coil currents shown, referred to as MF 6 9

Fig. 7. Magnetic field configuration generated in ET I by the coil currents shown, referred to as MF 7. 10

Fig. 8. Performance mapping of discharge efficiency versus mass utilization for several magnetic field configurations 12

Fig. 9. Langmuir probe current-voltage characteristic probe located 9 cm from cathode plane, 2.5 cm off-axis. Uniform magnetic field, ET I. 15

Fig. 10. Langmuir probe voltage-current characteristic probe located 12 cm from cathode plane, 5 cm off-axis 16

Fig. 11. Radial plasma density distribution derived from Langmuir probe measurements made in ET I. 19

Fig. 12. Radial plasma density distribution derived from Langmuir probe measurements made in ET I 12

Fig. 13. Radial potential distribution derived from Langmuir probe measurements made in ET I . 13

Fig. 14. Radial potential distribution derived from Langmuir probe measurements made in ET I . 14

Fig. 15. Schematic drawing of NASA-LeRC SERT II model discharge chamber showing magnetic field shape and axial field strength 27

Fig. 16. Performance mapping of NASA-LeRC SERT II model permanent magnet thruster for three cathode types 28

Fig. 17. Performance mapping of discharge efficiency versus mass utilization for variation of cathode position on discharge axis 33

Fig. 18. Mass utilization versus cathode-baffle spacing for ET II operated with a hollow cathode and the baffle shown 36

Fig. 19. Ion beam profiles measured with a Faraday cup probe in the beam of ET II . . . 37

Fig. 20. Performance mapping of ET II operated with a hollow cathode and a simple baffle located in optimum position 38

Fig. 21. Test of hollow cathode configuration 41

Fig. 22. Radial plasma density distribution according to eq. (19) 45

Fig. 23. Ionization rates of monoenergetic and Maxwellian electrons in mercury 54

Fig. 24. Energy loss rate of a Maxwellian distribution of electrons as a function of electron temperature in mercury 56

SECTION I

INTRODUCTION

The detailed behavior and mechanism of the crossed field discharge employed as an ion source in the Kaufman-type[1] electrostatic thruster are understood at present only in rather vague, qualitative terms. The objective of our research is to gain a better understanding of the discharge properties and their dependence on discharge parameters, and to use this understanding to optimize thruster performance. With this goal, the present program involves a study of the effects on the discharge properties of the magnetic field strength and configuration, the cathode location and type, and the method of propellant introduction. The discharge properties of interest are the plasma potential and density distributions; the electron, ion, and neutral energy distributions; and the electrical energy required to produce an extracted ion. These quantities are varied and studied under typical thruster operating conditions.

The over-all schedule of this research program can be divided into the following tasks:

Task I — Discharge Diagnostic Experiments

Task II — Discharge Optimization

Task III — Discharge Theory.

It is important to recognize that these tasks are not actually distinct and isolated, but interact in every phase. Diagnostics and optimization are being studied with several thruster configurations. The first configuration, a NASA-LeRC thruster of recent design, serves as a basis for comparison of performance. The second and third configurations (labeled "Experimental Thruster I" and "Experimental Thruster II") were constructed with the objective of providing as much flexibility as possible. They can accommodate a wide variety of magnetic field geometries, various locations for propellant introduction, and changes in location as well as type of cathode. One of these thrusters was designed primarily for diagnostic studies, and the other is intended for optimization studies.

The work reported herein will include performance mapping of the NASA-LeRC thruster, performance tests of ET I with oxide cathodes, diagnostics of ET I with oxide cathodes, and initial performance tests of ET II with hollow cathodes. The results of hollow cathode erosion tests in a diode configuration and the status of the theoretical effort are also reported.

SECTION II

DISCHARGE DIAGNOSTIC EXPERIMENTS

A. DESCRIPTION OF EXPERIMENTAL THRUSTERS

A thruster was designed for the experimental investigation of the discharge chamber; this thruster provides for relative ease in modification of the discharge chamber geometry and operating characteristics. This design has the following distinctive features:

- propellant feed system can be positioned for reverse, forward, or distributed propellant feed
- discharge chamber long enough to permit length-to-diameter ratio studies
- segmented solenoid can provide a variety of magnetic field configurations
- adaptable to diagnostic instrumentation.

The thruster is shown schematically in Fig. 1. The probe shown in the thruster schematic can be a Langmuir probe or a Faraday cup probe, or it can be removed and replaced by an auxiliary discharge cathode. The type of probe used in the diagnostic experiments is sketched, showing dimensions, in Fig. 2. Only two of the eight propellant feed tubes are shown in Fig. 1. These feed tubes may be made longer or inserted at other axial locations (reverse feed location is shown). Two of the thrusters have been constructed for use in both the diagnostic and optimization program; they will be referred to as ET I and ET II (Experimental Thrusters I and II). A typical operating point for ET I is as follows:

Discharge voltage	40 V
Discharge current	1.54 A
Discharge power	61.6 W
Discharge eV/extracted ion	255 eV/ion
Beam current	242 mA
Neutral current	268 mA (equivalent)
Mass utilization	90.3%

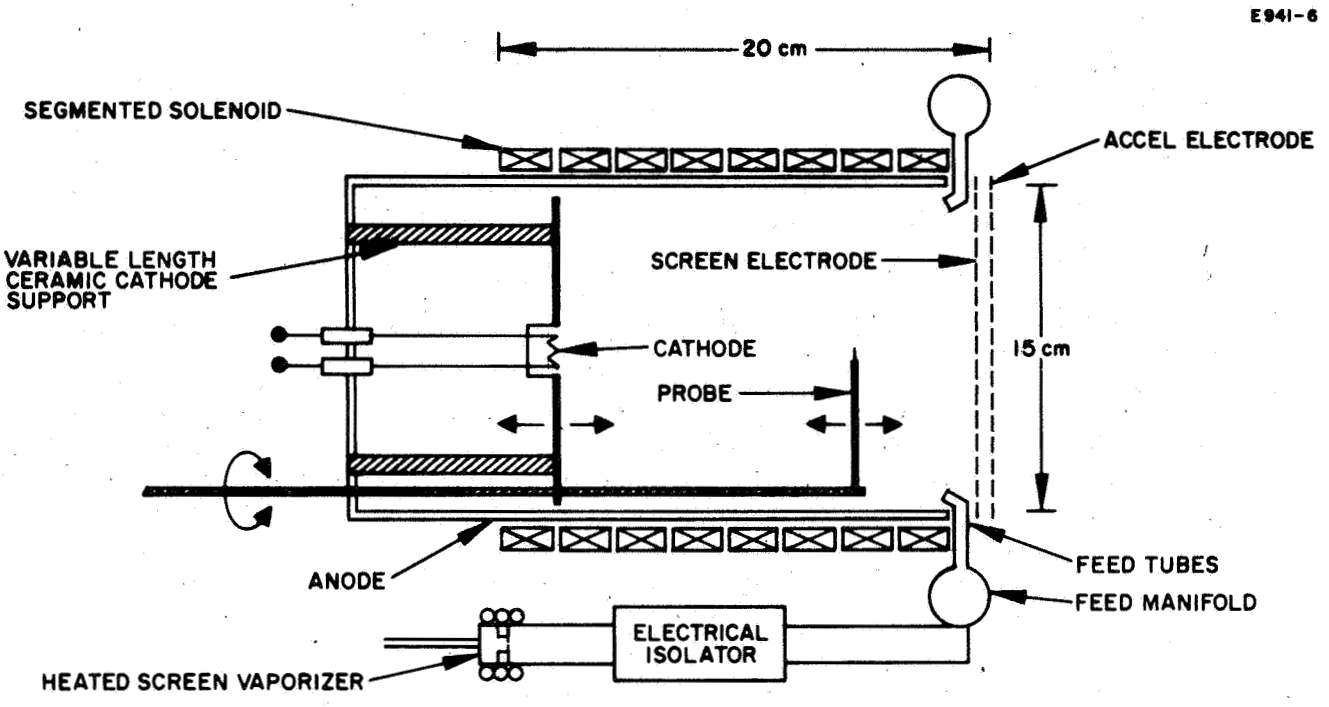

Fig. 1. Schematic drawing of the versatile experimental thruster used in diagnostic and optimization experiments.

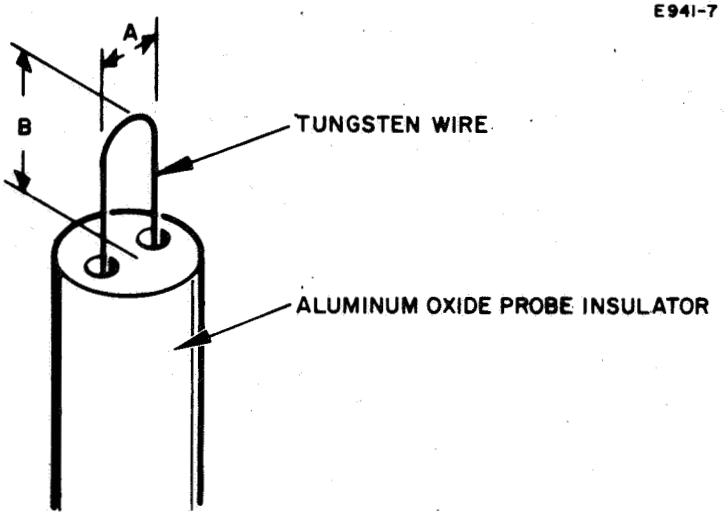

Fig. 2. Pictorial drawing showing dimensions of the Langmuir probe used in the experiments described in this report (may be used as a cold collecting probe or as an emissive probe).

Beam voltage	3 kV
Decelerating voltage	2 kV
Magnetic field	28 G
Cathode power	104 W.

These parameters were measured using a spiral (oxide) cathode located 13 cm from the screen electrode. The magnetic field coils were operated to provide a relatively uniform axial field. Neutral flow was determined by monitoring the change in mercury level in a calibrated pipette standpipe, which acts as the liquid mercury reservoir. The above parameters are more or less typical of the discharge of advanced electron bombardment thrusters; therefore we believe that the experimental discharge chambers employed here are representative for state-of-the-art thrusters.

B. MAGNETIC FIELD VARIATIONS AND THRUSTER PERFORMANCE

Effects of the magnetic field configuration were studied using various magnetic fields produced by the segmented solenoid for different current ratios in the windings. To give a graphic illustration of the shape of each magnetic configuration, a powdered iron "field map" was made. Figure 3 is a photograph of one such map made for the NASA-LeRC permanent magnet thruster magnetic field configuration. The procedure for making a powdered iron field map is quite simple. A piece of cardboard is cut to fit the discharge chamber, and powdered iron is scattered as uniformly as possible over its surface. The iron covered cardboard is then inserted carefully in the discharge chamber and tapped lightly until the pattern takes shape. The cardboard is then removed carefully and sprayed with a clear lacquer to preserve the pattern of the field map. Tracings of several field maps made in ET I are shown in Figs. 4 through 7. These figures show the effective field configuration and the currents in the coil segments which produce them. Since there is no pole piece used in producing these configurations, any set of currents in the same ratio will produce the same magnetic field configuration. The values of the axial component of the magnetic field are given for the currents shown. Figure 4 shows the most uniform field configuration and Fig. 7 the most divergent field configuration. The different magnetic field configurations will be referred to hereafter as MF 4, MF 5, MF 6, and MF 7.

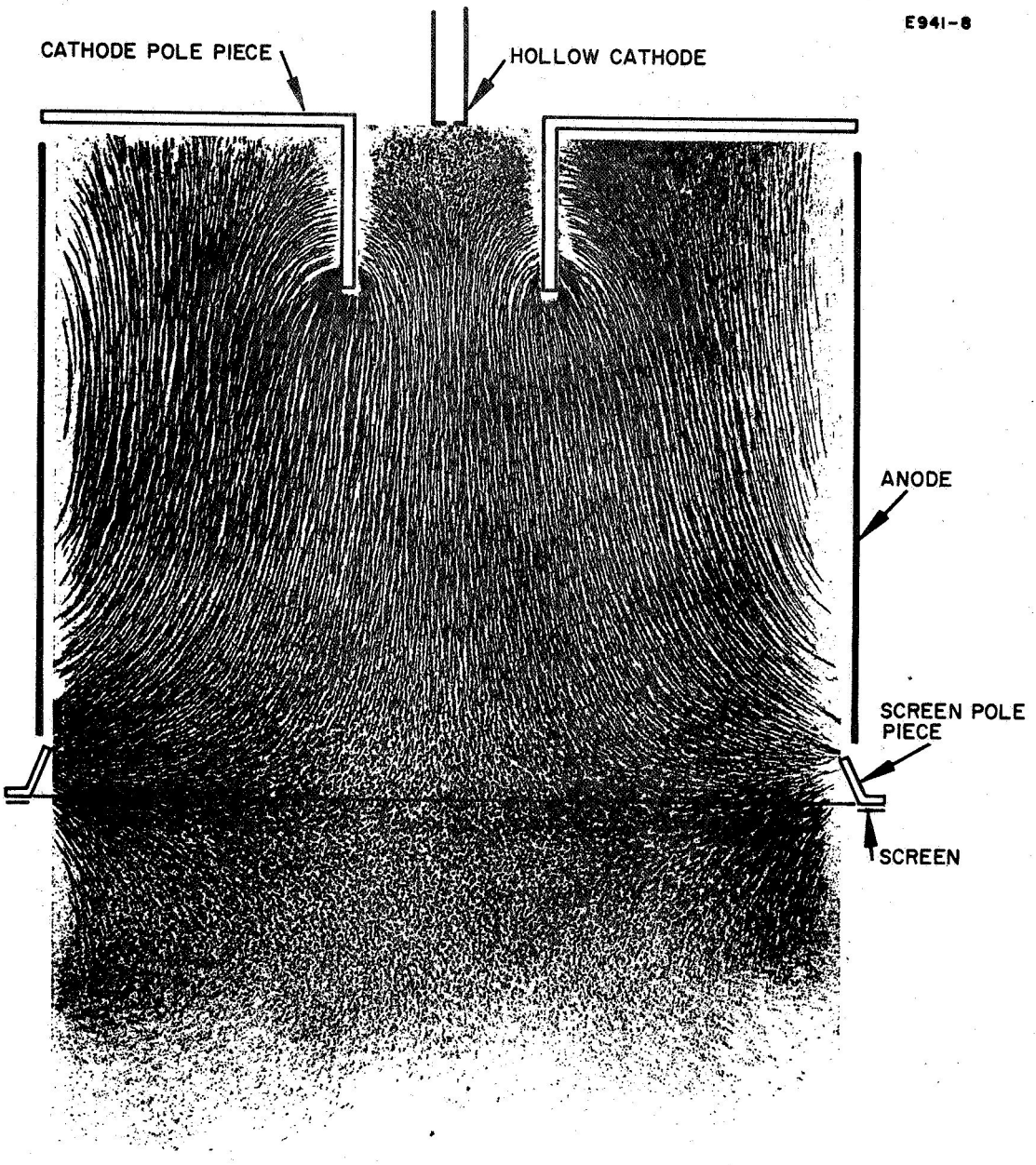

Fig. 3. Photograph of powdered iron field map of magnetic field configuration in a thruster discharge chamber. This map made in the SERT-II model, permanent thruster. (Discharge chamber electrodes are sketched.)

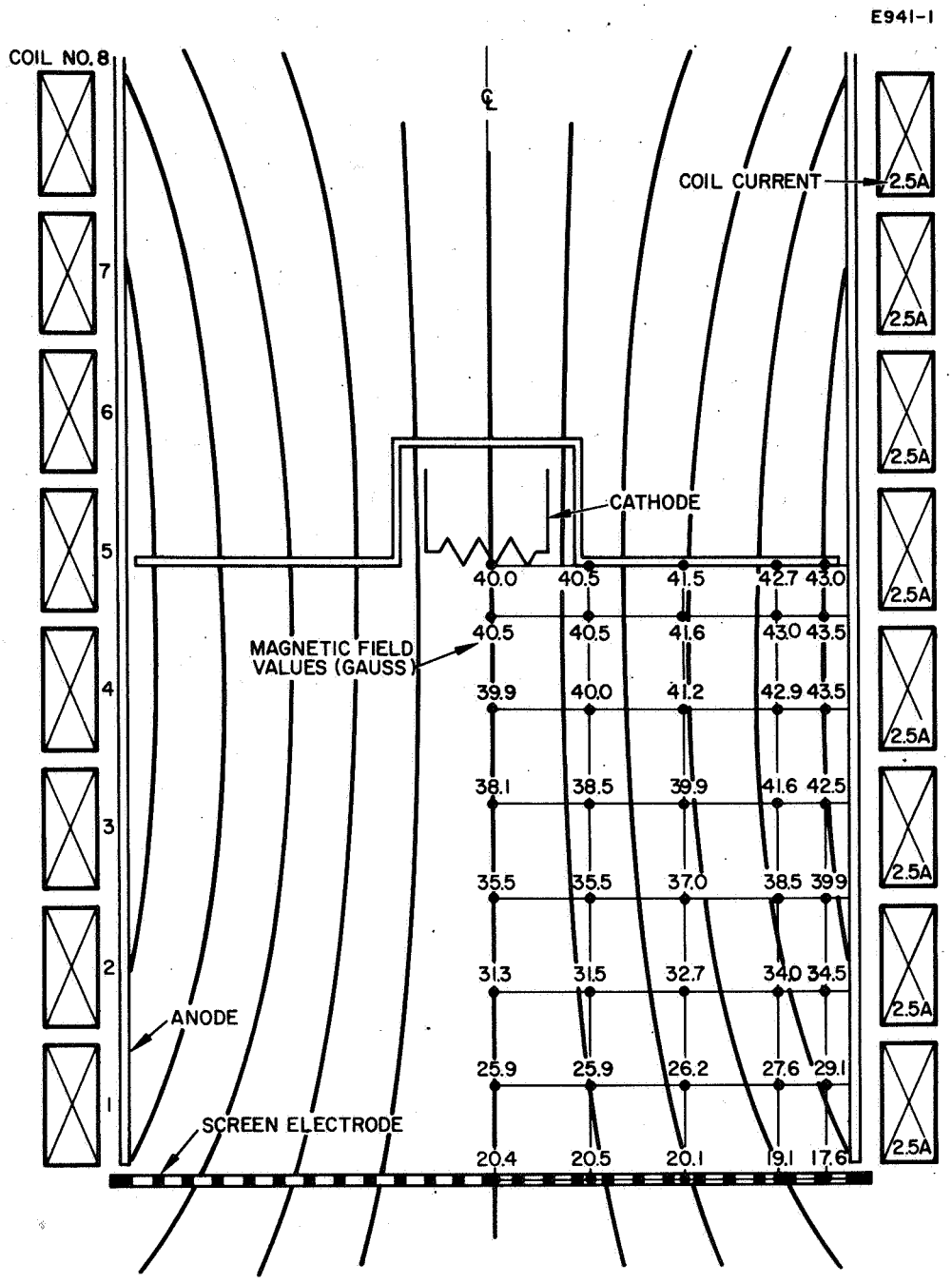

Fig. 4. Magnetic field configuration generated in ET I by the coil currents shown, referred to as MF 4. The field lines are tracings of a powdered iron field map such as that shown in Fig. 3. The magnetic field values shown are the axial component (measured with an axial Hall-effect probe gaussmeter).

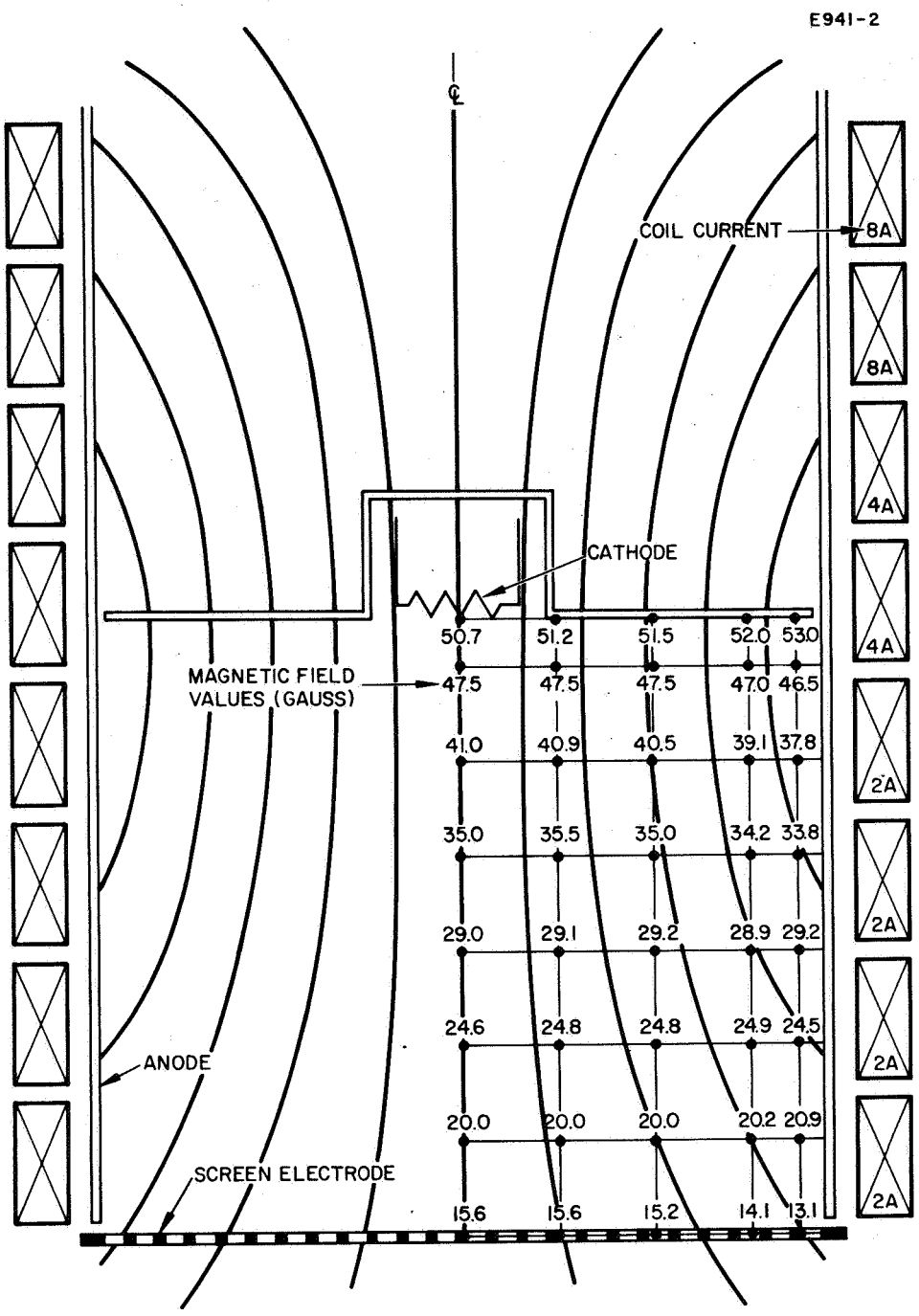

Fig. 5. Magnetic field configuration generated in ET I by the coil currents shown, referred to as MF 5. The field lines are tracings of a powdered iron field map such as that shown in Fig. 3. The magnetic field values shown are the axial component (measured with an axial Hall-effect probe gaussmeter).

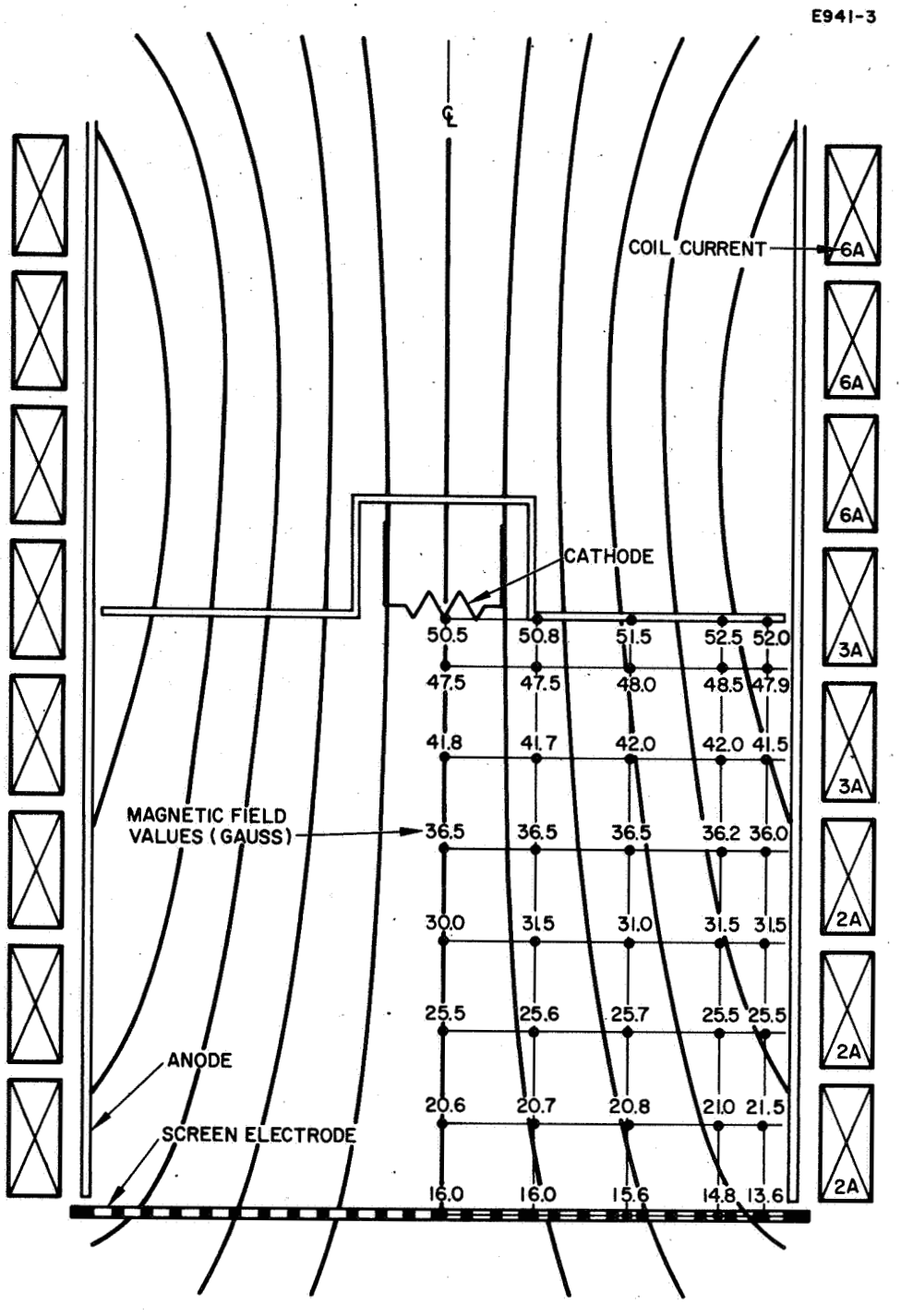

Fig. 6. Magnetic field configuration generated in ET I by the coil currents shown, referred to as MF 6. The field lines are tracings of a powdered iron field map such as that shown in Fig. 3. The magnetic field values shown are the axial component (measured with an axial Hall effect probe gaussmeter).

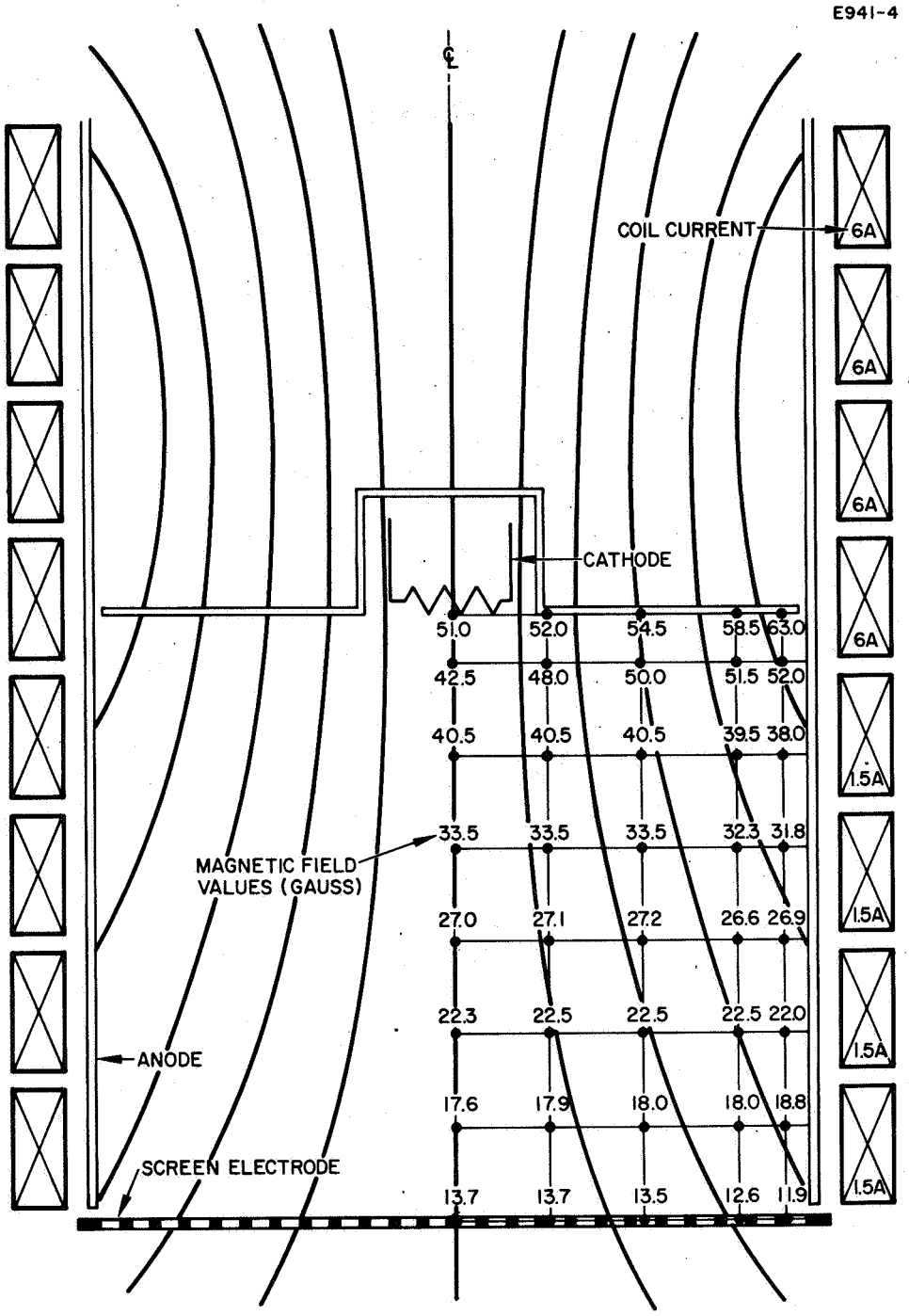

Fig. 7. Magnetic field configuration generated in ET I by the coil currents shown, referred to as MF 7. The field lines are tracings of a powdered iron field map such as that shown in Fig. 3. The magnetic field values shown are the axial component (measured with an axial Hall effect probe gaussmeter).

The performance for these magnetic configurations was mapped with the cathode power and neutral flow (reverse feed) into the engine constant and the discharge voltage (and consequently the discharge and beam currents) varied. For all magnetic configurations the beam current increases with magnetic field strength, eventually saturating at some value of the magnetic field. Performance mappings for magnetic field configurations MF 4, 5, 6, and 7 are shown in Fig. 8 (the magnet coil current ratios for these data are given in Table I). It can be seen that increasing the divergence of the magnetic field configuration tends to improve discharge efficiency (decrease the eV/ion) at any fixed mass utilization; however, increased divergence also limits the largest attainable mass utilization to a lower value. The most significant differences in performance characteristics are between MF 4 and MF 7, the configurations in which diagnostic (Langmuir probe) measurements have been made.

C. ANALYSIS OF LANGMUIR PROBE MEASUREMENTS

Several remarks should be made concerning the Langmuir probe technique before the results of the measurements are given. Langmuir probe measurements are subject to numerous sources of error, and the results may be questionable even under the most ideal conditions. Measurements in an operating ion engine discharge, which requires that the instruments float 3 kV above ground, are somewhat less than ideal, since they are influenced by all types of noise signals. Initially, 60 Hz pick-up from the power conditioning made measurements quite difficult. This type of noise was eliminated, and no other appreciable noise signal could be detected. When suitably reliable voltage-current probe characteristics are obtained, interpretation requires some hypothesis about the electron energy distribution in the plasma. Probe measurements made by Strickfadden and Geiler[2] in thruster discharges at JPL could be interpreted if the plasma was considered to have two types of electrons — a Maxwellian component with an average energy of several electron volts, and a component of monoenergetic primaries with energies of the order of the discharge voltage. Under this assumption, the Maxwellian component of the probe current can be expressed as

$$i_m = An_m e\left(\frac{kT}{2\pi m}\right)^{1/2} \exp\left(\frac{eV}{kT}\right), \quad V < 0, \qquad (1)$$

where

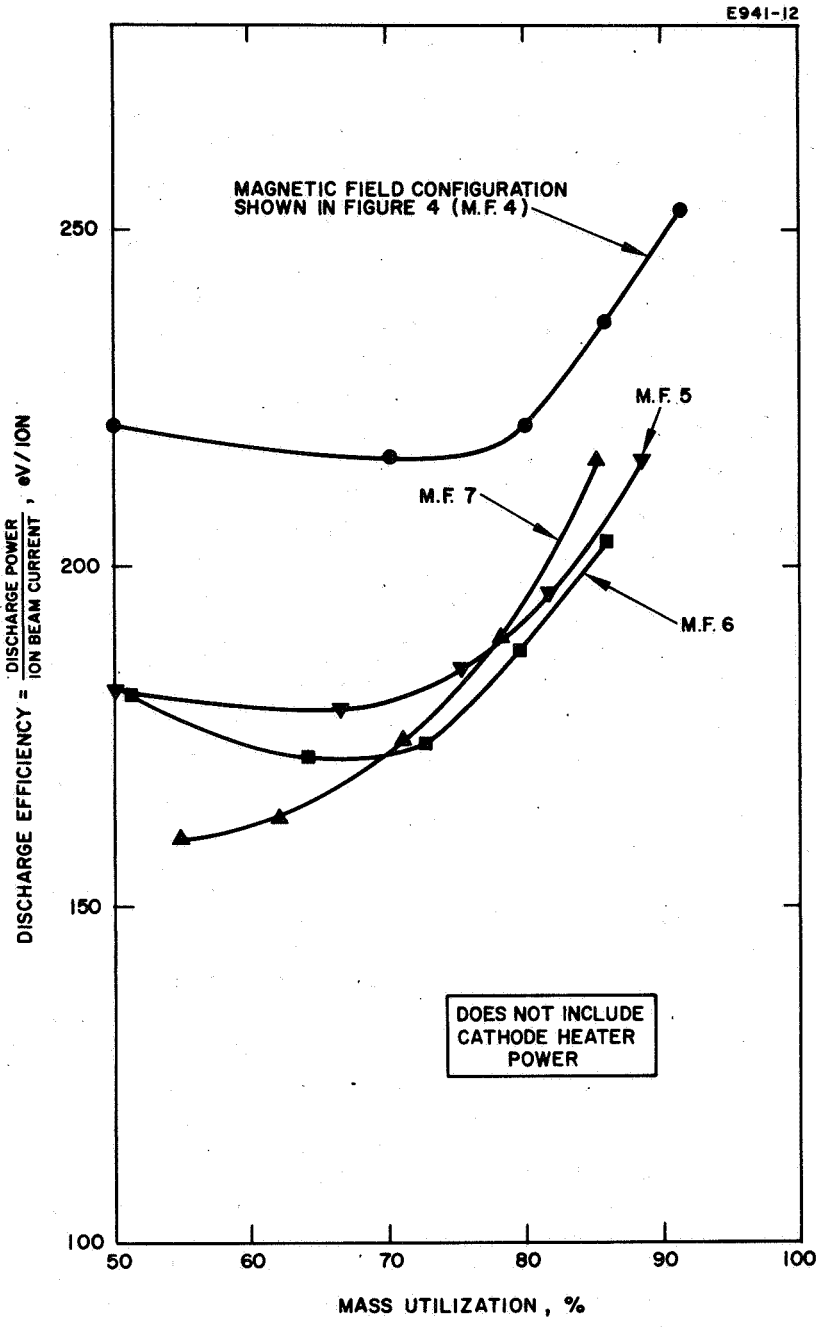

Fig. 8. Performance mapping of discharge efficiency versus mass utilization for several magnetic field configurations. Thruster parameters given in Table I.

TABLE I

Thruster Parameters for Data Shown in Fig. 8

○ Magnetic configuration of Fig. 4 (MF 4)
Magnet current = 2.5 A each coil
Cathode heater voltage = 4.75 V
Cathode heater current = 29 A
Equivalent neutral current = 282 mA

Arc Discharge			Ion Beam Performance					
V_D, V	I_D, A	P_D, W	V_{acc}, kV	V_{dec}, -kV	I_{beam}, mA	I_{drain}, mA	η_m, %	eV/Ion
45	1.45	65.2	4	1	258	0.65	91.5	253
40	1.43	57.2	4	1	242	0.7	85.8	236
35	1.43	50	4	1	226	0.7	80.2	221
30	1.43	42.9	4	1	198	0.8	70.2	216
25	1.25	31.2	4	1	141	0.85	50	221

□ Magnetic configuration of Fig. 6 (MF 6)
Magnet coil currents = 6, 6, 6, 3, 3, 2, 2, 2 A
Cathode heater voltage = 4.75 V
Cathode heater current = 29 A
Equivalent neutral current = 282 mA

Arc Discharge			Ion Beam Performance					
V_D, V	I_D, A	P_D, W	V_{acc}, kV	V_{dec}, -kV	I_{beam}, mA	I_{drain}, mA	η_m, %	eV/Ion
45	1.1	49.4	4	1	242	0.8	85.8	204
40	1.05	42	4	1	224	0.8	79.5	188
35	1.05	36.8	4	1	205	0.8	72.7	174
30	1.04	31.2	4	1	181	0.85	64.2	172
26	0.95	24.8	4	1	145	0.9	51.4	171

▽ Magnetic configuration of Fig. 5 (MF 5)
Magnet coil currents = 8, 8, 4, 4, 2, 2, 2, 2 A
Cathode heater voltage = 4.75 V
Cathode heater current = 29 A
Equivalent neutral current = 282 mA

Arc Discharge			Ion Beam Performance					
V_D, V	I_D, A	P_D, W	V_{acc}, kV	V_{dec}, -kV	I_{beam}, mA	I_{drain}, mA	η_m, %	eV/Ion
45	1.2	54	4	1	250	0.8	88.7	216
40	1.13	45.2	4	1	231	0.8	81.9	196
35	1.12	39.2	4	1	212	0.8	75.2	185
30	1.12	33.6	4	1	188	0.85	66.7	179
25	0.98	24.4	4	1	142	0.9	50.4	172

△ Magnetic configuration of Fig. 7 (MF 7)
Magnet coil currents = 6, 6, 6, 6, 1.5, 1.5, 1.5, 1.5, A
Cathode heater voltage = 4.75 V
Cathode heater current = 29 A
Equivalent neutral current = 282 mA

Arc Discharge			Ion Beam Performance					
V_D, V	I_D, A	P_D, W	V_{acc}, kV	V_{dec}, -kV	I_{beam}, mA	I_{drain}, mA	η_m, %	eV/Ion
45	1.15	35	4	1	240	0.8	85.2	216
40	1.05	28.5	4	1	224	0.8	78.3	190
35	1.0	24.8	4	1	200	0.8	71	175
30	0.95	49.4	4	1	175	0.9	62.1	163
27.5	0.9	42	4	1	155	0.95	55	160

A ≡ collecting area of the probe

T ≡ electron temperature of the Maxwellian component of the plasma electrons

n_m ≡ density of Maxwellian electrons

V ≡ probe potential measured with respect to plasma potential.

For the primary electrons, we assume an ensemble of monoenergetic electrons with energy eV_{pr} and with randomly directed velocities. Langmuir[3] has shown that for retarding potentials ($V \leq 0$), the current to a probe of any geometry is then given by

$$i = i_{pr} = An_{pr}e\left(\frac{2eV_{pr}}{m_e}\right)^{1/2}\left(1 + \frac{V}{V_{pr}}\right), \quad -V_{pr} \leq V \leq 0 \tag{2}$$

where

V ≡ potential of the probe relative to the space (plasma) potential

n_{pr} ≡ density of primary electrons with energy eV_{pr}.

If $eV_{pr} >> kT$, it is relatively simple to separate primary and Maxwellian components, because the probe current at large retarding potentials is predominantly the primary current and is a linear function of the probe voltage. The voltage-current characteristic at large retarding potentials can be examined to determine and extract the primary component, as expressed by (2), leaving the Maxwellian current versus voltage. If the latter then is plotted semilogarithmically versus V, a straight line should result; its slope should yield kT in the customary way.

While this technique is successful in reducing some of the data obtained in ET I, other probe characteristics cannot be reduced in this way. For example, Figs. 9 and 10 show probe voltage-current characteristics for both situations. The curve in Fig. 9 lends itself readily to the two electron species interpretation. The original probe curve (dots) appears to have two "linear" regions (1 and 2); it is tempting to interpret this characteristic as arising from two Maxwellian distributions — two distinct species of electrons with temperatures corresponding to slope 1 (6.8 eV) and slope 2 (10.2 eV). If the measured probe characteristic is plotted on a linear scale, it is apparent that the points below 26 V lie in a straight line which obeys the equation

$$i_{pr} = 0.2\,(V-12)\ \text{mA} \quad \text{when} \quad V \leq 46\ \text{V}; \tag{3}$$

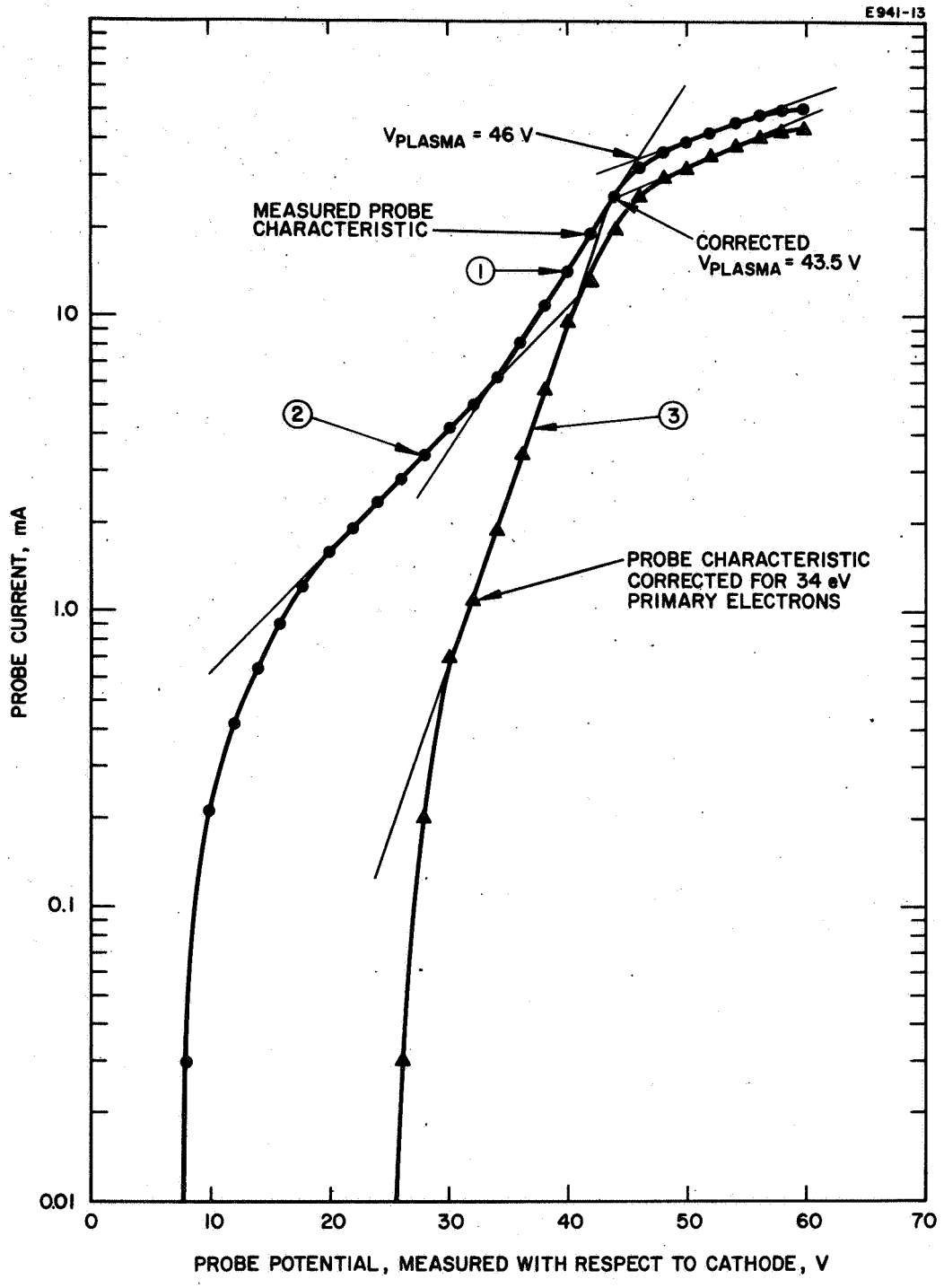

Fig. 9. Langmuir probe current-voltage characteristic probe located 9 cm from cathode plane, 2.5 cm off-axis, uniform magnetic field, ET I.

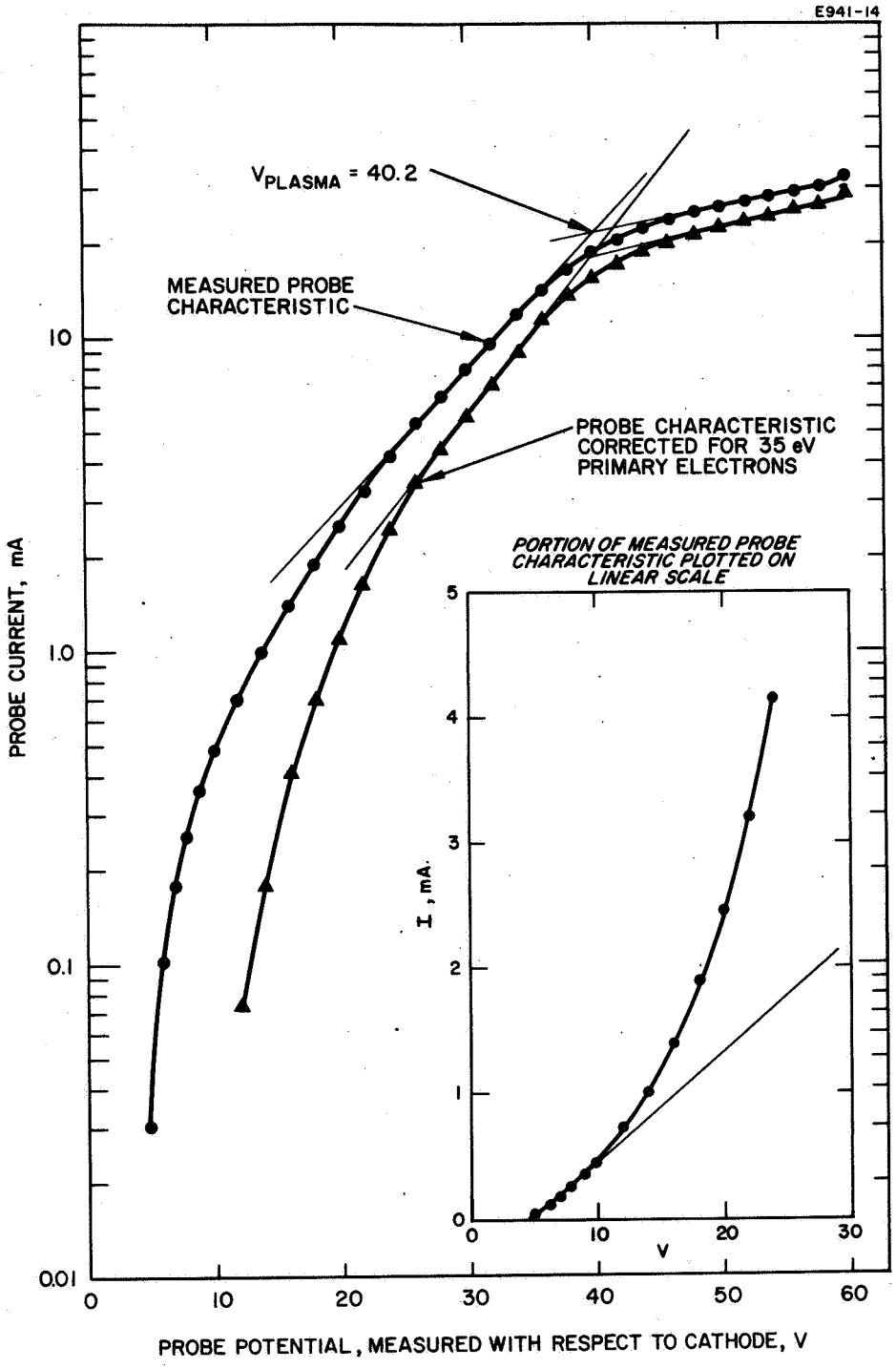

Fig. 10. Langmuir probe voltage-current characteristic probe located 12 cm from cathode plane, 5 cm off-axis. Uniform magnetic field, ET I.

Here V is measured with respect to the discharge cathode, yielding V_{pr} = 34 V. Using eq. (3), the primary component of the probe current is computed for each data point and deducted from the measured current value, thus "correcting" for the contribution of primary electrons to the probe current. When this correction is performed for the probe characteristic shown with dots in Fig. 9, the characteristic shown with triangles is obtained. The slopes of the uncorrected curves in Fig. 9 (labeled 1 and 2) cover less than an order of magnitude in current change. However, the corrected curve (slope 3) is linear over a full order of magnitude and yields a revised electron temperature of 3.9 eV. The plasma potential indicated by the "saturation" of the probe current is also shifted somewhat. The electron density computed from the electron saturation current and the electron temperature is found to be 4.4×10^{11} cm^{-3} for either curve in this case. It has been found empirically that as long as the upper slope (corresponding to 1 of Fig. 9) is used to determine electron temperature for the density computation, the value of the density differs insignificantly from that obtained when the characteristic is "corrected" for primary electrons. To associate a "temperature" with the linear region of the probe characteristic, the linear region should cover several orders of magnitude change in probe current. Although none of the characteristics which have been measured possess this property, the correctable characteristics (as in Fig. 9) display a linear region over at least an order of magnitude.

Figure 10 shows a probe characteristic for which the above described data "correction" procedure fails. A small region of the characteristic could be considered linear, but the "temperature" derived from the slope in this region is somewhat higher (11 eV) than might be expected. This may result from the presence of a high energy electron population which is neither monoenergetic nor Maxwellian. Because correction of this type of data is not possible, spatial distributions of electron energy cannot be obtained from probe measurements. However, plasma potential and electron density can be obtained from these curves to within an estimated accuracy of 10%. Plasma potential is obtained — in the conventional manner — from the intersection of the asymptote drawn through the "linear" section and the "saturation" section of the probe characteristic. For characteristics such as those of Fig. 9, the "corrected" characteristics are used; for those such as Fig. 10, the measured characteristic is used. The "saturation" current required to obtain plasma density is then taken to be the probe current at plasma potential, and it can be read directly from the probe voltage-current characteristic. For characteristics such as those shown in Fig. 9 (corrected characteristics), the plasma density is obtained in a straightforward way from eq. (1) because V = 0 at plasma potential and T is easily determined from the slope of the linear region of the semilog plot. For characteristics such as those

shown in Fig. 10, one can assume only that this same procedure is valid (i.e., that the "saturation" current can be related to the density through eq. (1), and that the "temperature" derived from the quasi-linear, upper portion of the probe characteristic is representative of the average arrival rate of electrons at the probe — because T_e is necessary in the use of eq. (1)). The only justification which can be offered for applying this procedure to such characteristics as those in Fig. 10 is that the results presented below appear reasonable. While primary electrons which obey eq. (2) may contribute appreciably to the probe current, their densities (in the probe data obtained here) may be neglected because of their relatively high velocities.

D. LANGMUIR PROBE MEASUREMENTS IN THE THRUSTER DISCHARGE

Langmuir probe measurements were made at 28 locations in ET I for operation with a uniform (MF 4) and a divergent (MF 7) magnetic field configuration. For these measurements, discharge voltage, cathode power, and neutral flow were kept constant at 40 V, 145 W, and 280 mA (equivalent), respectively. Beam and discharge current were observed to vary somewhat, depending on probe location, indicating that the probe disturbs the discharge operation somewhat (in all cases less than 10%).

The radial plasma density distributions obtained from reduction of the Langmuir probe characteristics are seen in Figs. 11 and 12 with axial location as a parameter. (The insert in Fig. 11 shows to scale the relative location of the data points, and Fig. 2 showed the probe geometry and dimensions.) When the thruster is operated with a uniform magnetic field configuration, the density distribution is seen to peak near the center of the discharge chamber, dropping sharply in a radial direction and less sharply in the axial direction. Operation with a divergent (MF 7) magnetic field configuration displays a more uniform density distribution, which drops off less sharply in both directions. Figures 13 and 14 show the radial plasma potential distribution, with axial location as a parameter, for the same magnetic configurations. There appears to be little difference in the potential distribution in these two cases, and the scatter in the data points is more pronounced than in the density distributions. This can be attributed partly to the variation in probe characteristics at different locations, as seen in Figs. 9 and 10 and discussed earlier. The dependence on location probably results from a varying magnetic linkage between probe and cathode, which affects the ability of primary electrons from the cathode to pass directly to the probe along magnetic field lines. This point has not yet been clarified entirely, however. At this time it can be stated only that probe characteristics of

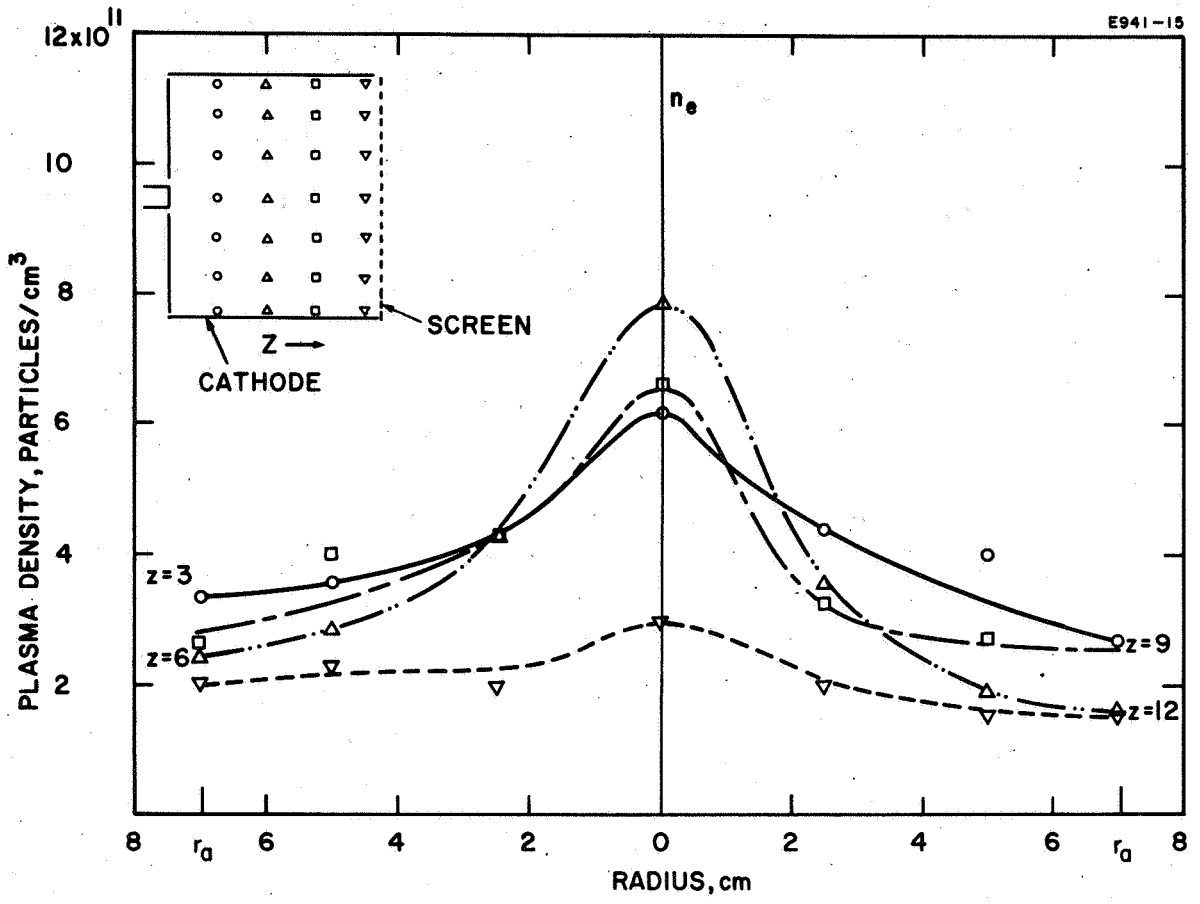

Fig. 11. Radial plasma density distribution derived from Langmuir probe measurements made in ET I. The thruster was operated with a spiral oxide cathode and a uniform magnetic field configuration MF 4. Z is the distance from the cathode to the plane of measurement (in centimeters) as shown in the diagram.

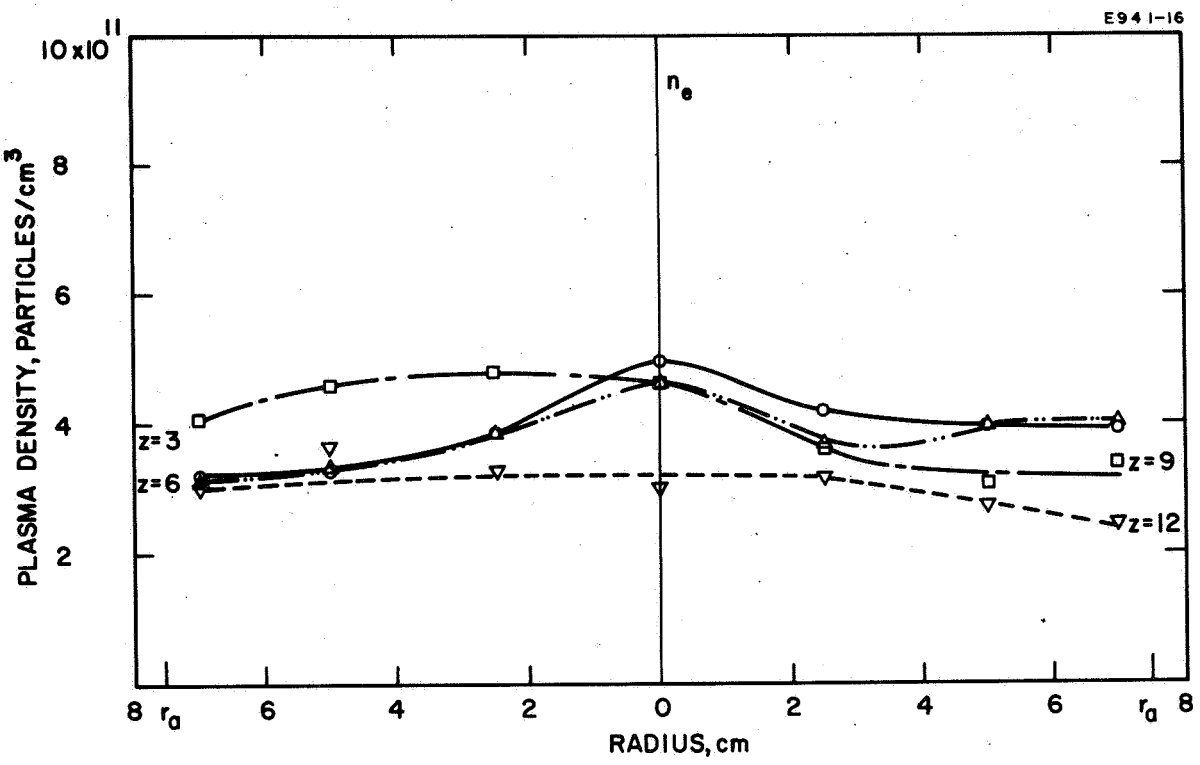

Fig. 12. Radial plasma density distribution derived from Langmuir probe measurements made in ET I. The thruster was operated with a spiral oxide cathode and a divergent magnetic field configuration MF 7. Z is the distance from the cathode to the plane of measurement.

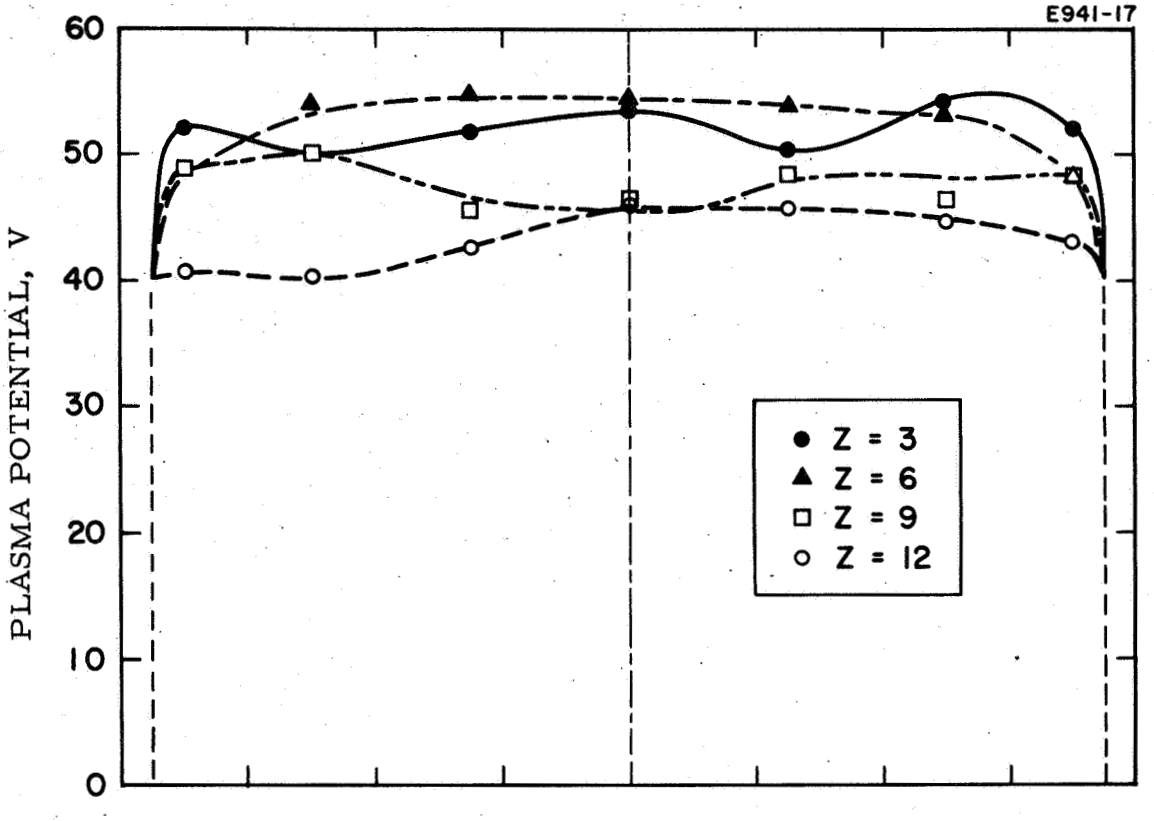

Fig. 13. Radial potential distribution derived from Langmuir probe measurements made in ET I. The thruster was operated with a spiral oxide cathode and a uniform magnetic field configuration MF 4. Z is the distance from the cathode to the plane of measurement (in centimeters).

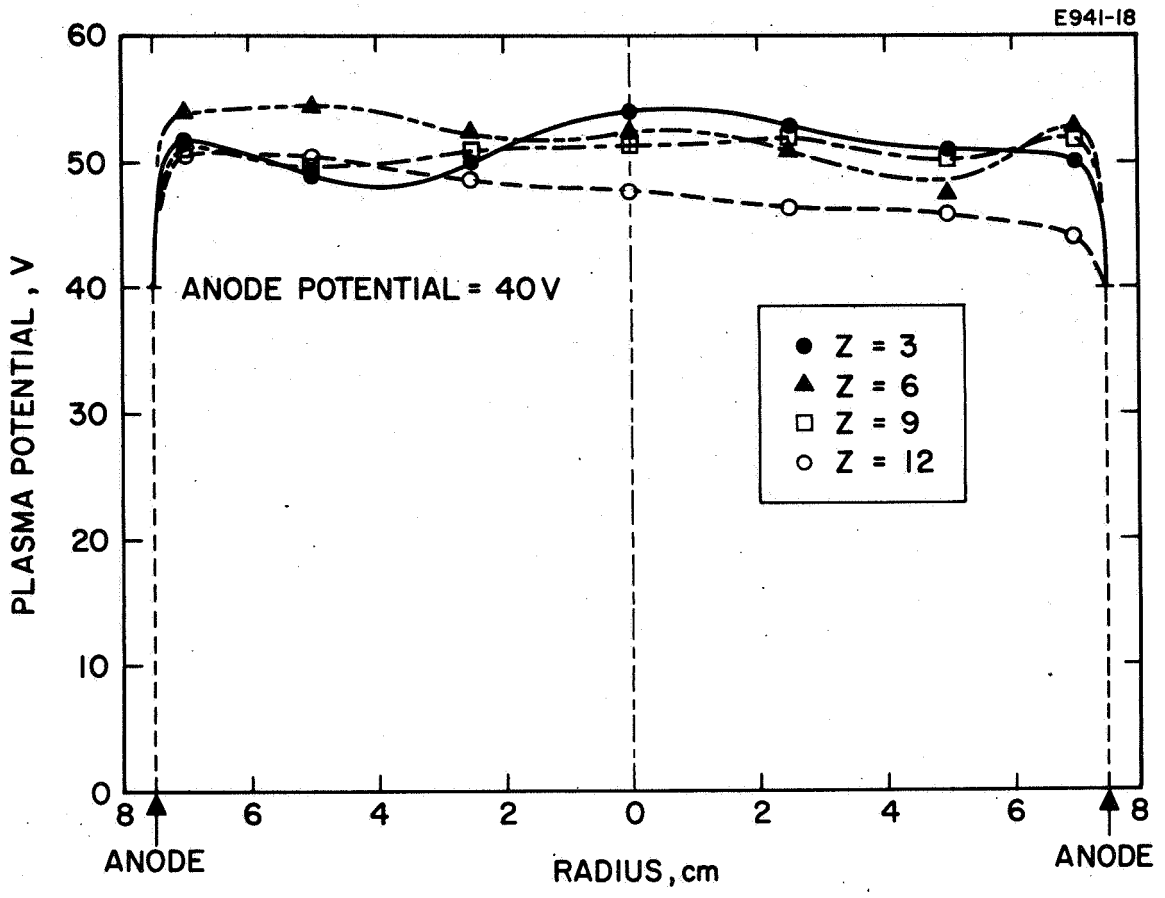

Fig. 14. Radial potential distribution derived from Langmuir probe measurements made in ET I. The thruster was operated with a spiral oxide cathode and a divergent magnetic field configuration MF 7. Z is the distance from the cathode to the plane of measurement (in centimeters).

the type seen in Fig. 10 are measured in the vicinity of the cathode and the screen electrode, and are more pronounced (difficult to find a linear region) near the discharge axis. While the interpretation of the semilog slope of these characteristics as temperature is questionable, it is interesting to note that these slopes yield temperatures of 5 to 15 eV, while the characteristics which are corrected for primaries (as in Fig. 9) yield temperatures of 1 to 5 eV. In order to clarify this apparent contradiction, measurements will be made with a Faraday cup probe which will provide a total energy spectrum of the plasma electrons. After this technique has been tested, further studies of the effects of magnetic configuration will be made using configurations involving iron pole pieces, such as the magnetic configuration of the NASA-LeRC thruster.

SECTION III

OPTIMIZATION

The results reported in this section are principally measurements of thruster performance made with different thruster configurations or conditions. No attempt is made to vary all possible parameters; those parameters which seem to affect performance most are varied systematically. The performance characteristics reported at this stage of the program include tests made in the NASA-LeRC SERT II permanent magnet thruster with each of three cathode types, tests made in an experimental thruster (ET II) with a variable position cathode, and in ET II with a hollow cathode and a variable position baffle.

The NASA-LeRC SERT II model permanent magnet thruster is somewhat unique because of its highly divergent magnetic field configuration. The discharge chamber is shown schematically in Fig. 15 with the axial magnetic field values given at a number of points in the chamber. Propellant enters the chamber through orifices located around the periphery of the back wall of the discharge chamber on a diameter slightly larger than that of the cathode pole piece (or through-feed). Using a set of 70% transparent optics,* performance mapping experiments were undertaken with a NASA magazine type oxide cathode, a spiral nickel-oxide coated cathode, and a hollow or discharge cathode. Figure 16 shows a performance mapping (taking account of discharge power only) for this thruster with the three cathode types (thruster parameters are given in Table II). Table III gives a typical operating point for the thruster with each of the three cathode types. It can be seen from Table III that although the discharge efficiency is best for operation with the spiral oxide cathode, the over-all ion production efficiency is much better for operation with the hollow cathode than with either of the oxide cathodes, because of the relatively large heater power required with oxide cathodes.

The performance of this discharge chamber depends rather critically on the location of the cathode in the cathode pole piece, probably because of the shape of the magnetic field. When the thruster is operated with an oxide cathode, the emitting surface must be within several millimeters of the front face of the pole piece. When the thruster is operated with the hollow cathode, the cathode orifice is located in the rear plane of the cathode pole piece, and a baffle (which diverts the propellant introduced through the hollow cathode) is positioned in the plane of the front face of the pole piece. The hollow cathode is started by means of an auxiliary electrode which is called a keep-alive, or keeper. This electrode is simply a wire which is bent in a circular shape and located coaxially with, and approximately 0.060 in. in front of, the front face of the hollow cathode body. The role of the keep-alive

*NASA TM X-52326, Table II, Grid Set No. VI.

discharge in determining thruster performance and cathode lifetime (erosion) is not yet certain, but it is known to affect both. Some cathode erosion was noted during the relatively short thruster operation (30 to 40 hours). As a result, controlled hollow cathode erosion experiments (described later in this report) were performed, and the degree or lack of erosion was found to be related to the keep-alive discharge conditions; however, the details of this relation between keep-alive discharge conditions and cathode erosion are not yet determined. Preliminary experiments were also performed to determine the effect of this discharge on thruster discharge performance. Thruster performance was found to decrease (ion beam current decreases) when the keep-alive discharge voltage was reduced to zero. Restoring ion beam current by increasing the thruster discharge activity (increasing discharge current by increasing discharge voltage) results in a decrease in discharge efficiency of 50 eV/ion; in contrast, the cost of operating the keep-alive discharge (before the keep-alive voltage is reduced to zero) is only 25 eV/ion. The role of the keep-alive discharge will be studied further.

Several qualitative comparisons can be made between hollow cathode and oxide cathode thruster operation. The discharge voltage is nearly constant over a rather large range of discharge currents in a thruster operated with a hollow cathode, while a relatively wide range of voltages and currents is possible with oxide cathode thruster operation. This indicates that the discharge characteristics (plasma density, potential, and electron energy distributions) may be entirely different. To investigate this possibility, probe measurements are planned for the near future for a thruster operated with a hollow cathode. In addition, it was increasingly difficult to start the hollow cathode after exposure to atmosphere, and mass utilization greater than 90% could not be achieved.

Any attempt at a complete analysis of thruster discharge operation would be premature at this time, but several observations should be made. From the plasma density distributions measured in magnetic configuration studies with ET I, it is reasonable to conclude that the relatively good performance of the NASA thruster arises from the relatively uniform plasma density distribution associated with extreme divergence of the magnetic field. It is probable that the density distribution there is more uniform because the primary electrons can travel radially outward from the cathode along the divergent field lines, thus increasing the volume of the region of primary ionization. As a result the number of primaries per unit volume decreases somewhat in this region, but the total number of ionizations does not. Consequently, a spatially more uniform plasma of decreased density should result. Since the plasma in the divergent magnetic field discharge chamber has smaller radial density gradients, radial diffusion of ions toward

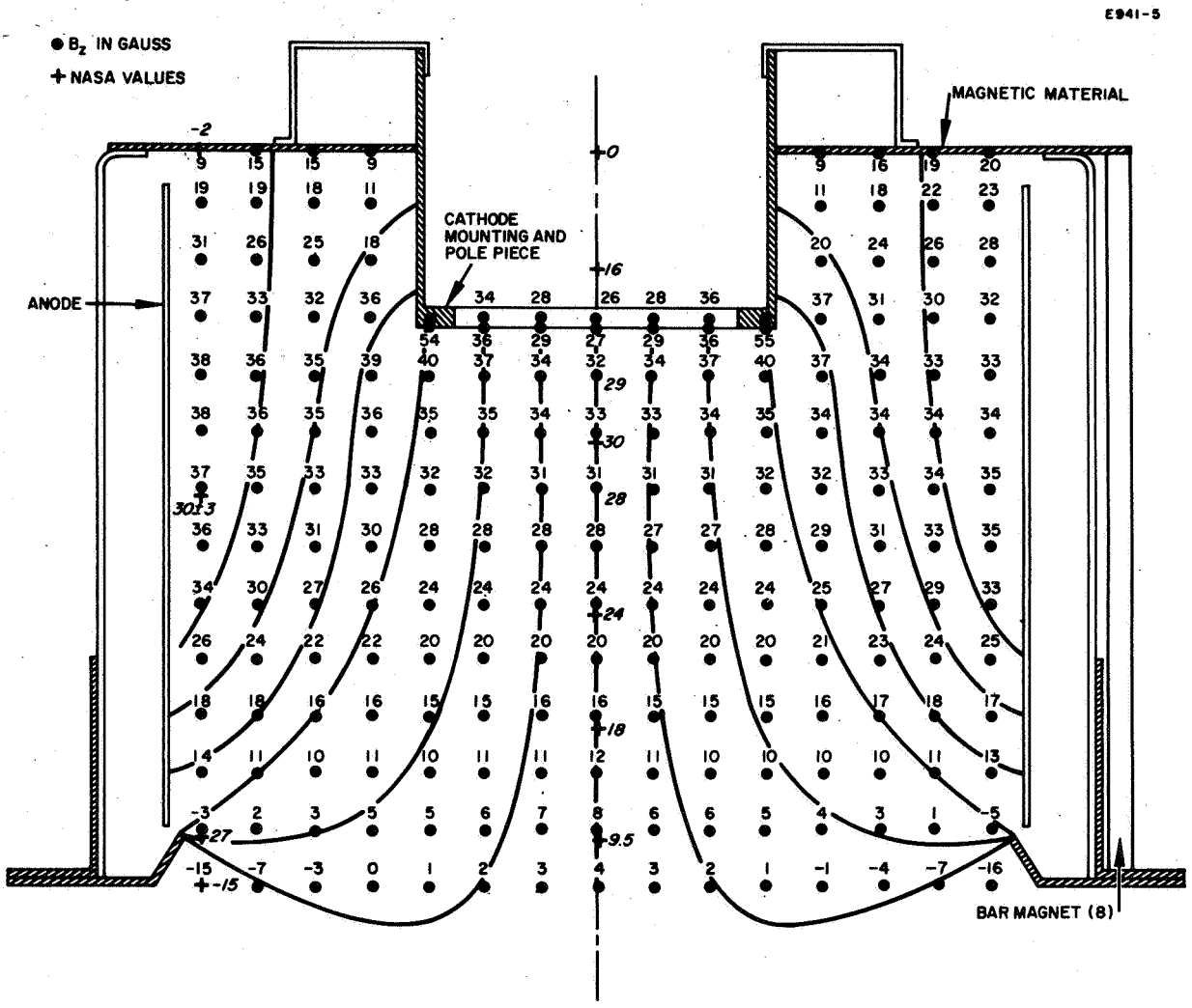

Fig. 15. Schematic drawing of NASA-LeRC II model discharge chamber showing magnetic field shape and axial field strength.

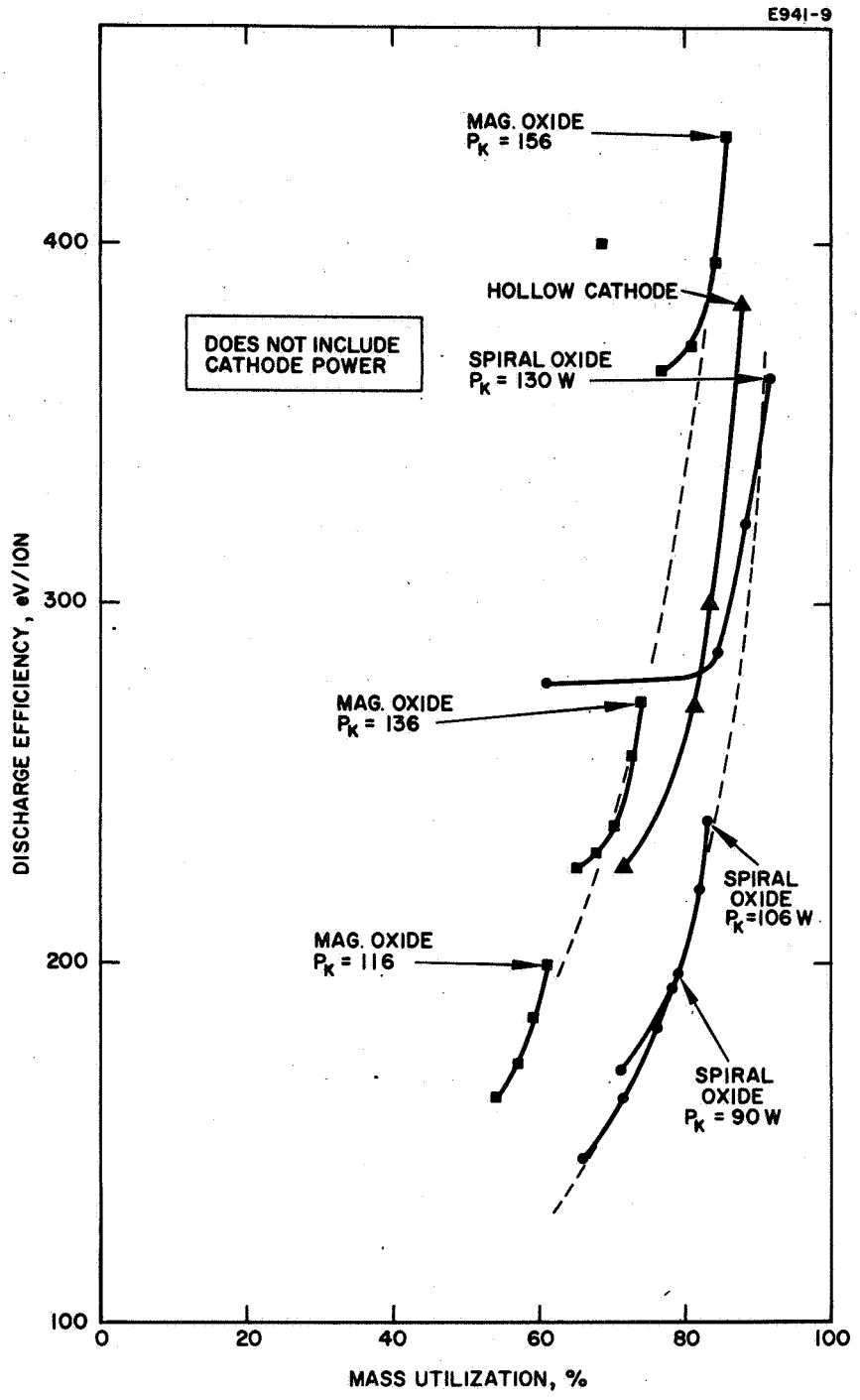

Fig. 16. Performance mapping of NASA-LeRC SERT II model permanent magnet thruster for three cathode types. (Thruster data given in Table II).

TABLE II

Thruster Parameters for Performance Mapping of NASA-LeRC SERT II Model Thruster Operated with Spiral and Magazine Type Oxide Cathodes and a Hollow (Discharge) Cathode, shown in Fig. 16

Spiral Oxide Cathode, Equivalent Neutral Current = 290 mA, Vacuum Chamber Pressure = 3×10^{-7} Torr									
Cathode Heater			Arc Discharge			Ion Beam Performance			
V_K, V	I_K, A	P_K, W	V_D, V	I_D, A	P_D, W	I_{beam}, mA	I_{drain}, mA	η_m, %	eV/Ion
3.6	36	130	40	2.4	96	265	0.9	91.6	362
			35	2.35	82.4	255	1.1	88	323
			30	2.35	70.5	245	1.2	84.5	287
			25	1.95	48.7	175	1.4	60.5	278
3.2	33	106	40	1.5	60	240	1.0	83	240
			35	1.5	52.5	221	1.1	82.3	221
			30	1.45	43.5	193	1.3	77.8	193
			25	1.4	35	171	1.5	71.0	171
3.0	30	90	45	1.0	45	228	1.0	78.8	197
			40	1.0	40	220	1.2	76	182
			35	0.95	33.2	205	1.4	71	162
			30	0.92	27.6	190	1.7	65.6	145
Magazine Oxide Cathode, Equivalent Neutral Current = 306 mA									
4.2	37	156	49	2.3	113	263	0.7	85.8	430
			45	2.25	101.5	257	0.75	83.8	395
			40	2.3	92	247	0.8	80.6	372
			35	2.4	85.8	235	0.9	76.6	365
			30	2.8	84	210	1.05	68.6	400
3.9	35	136	50	1.25	62.5	229	0.8	74.2	273
			45	1.27	57.2	222	0.8	72.5	258
			40	1.28	51.2	215	0.85	70.2	238
			35	1.37	48	208	0.9	67.8	231
			30	1.5	45	198	0.9	64.6	227
3.5	33	116	50	0.75	37.5	187	1.0	61.1	200
			45	0.75	33.7	182	1.0	59.4	185
			40	0.75	30	175	1.0	57	172
			36	0.75	27	165	1.05	53.9	163
Hollow Cathode, Equivalent Neutral Current = 308 mA, 272 mA through Main Feed System, 36 mA through Hollow Cathode, Cathode Heater = 5.2 V, 8 A, 41.6 W									
12.3	0.42	5.2	32.4	3.2	103.8	270	2.0	87.7	384
13.1	0.43	5.6	32	2.4	76.8	256	2.2	83.2	300
13.6	0.43	5.9	32	2.1	67.2	249	2.3	81	269
14	0.43	6.0	31.8	1.58	50	220	2.4	71.5	227

TABLE III

Typical Operating Points

Cathode	V_{acc}, kV	V_{dec}, kV	I_{beam}, mA	η_{mass}, %	$P_{cathode}$, W	$V_{discharge}$, V	$I_{discharge}$, A	eV/ion (discharge)	V_{keeper}, V	I_{keeper}, A	eV/ion (total)
Spiral (oxide)	3	2	225	78	106	30	1.45	193	—	—	678
Magazine (oxide)	3	2	250	76	144	30	2.25	270	—	—	805
Hollow	3	2	250	81.3	31	32.4	2.05	264	13	0.43	412

the wall (anode) should be reduced and discharge efficiency should be increased. It is also reasonable to conclude that the absence of the very dense plasma in the center of the divergent field discharge chamber allows more neutral atoms to traverse the thruster chamber without being ionized; therefore, the mass utilization should be expected to be somewhat lower. If this analysis is correct, optimum performance should be attained in a geometry (magnetic field) which distributes the primary electrons more or less uniformly over the ion extraction surface. Furthermore, neutral injection should occur from a location which requires that the neutral atoms travel a relatively long path across the plasma before they escape from the chamber. While the NASA thruster provides a magnetic configuration which meets the first requirement, the neutral injection used by this thruster may allow too many neutrals to escape.

To determine the effect of the location of the cathode in the discharge chamber, a variable position oxide cathode was installed in ET II in the same manner as the Langmuir probe seen in Fig. 1. For this experiment, the cathode shown in Fig. 2 was covered and the discharge cathode was mounted in place of the Langmuir probe on the probe positioning assembly. This cathode is an S-shaped, oxide coated nickel ribbon with an emitting area of 9.5 cm^2. The experiments were performed with the discharge power, cathode power, and neutral injection kept constant, and the beam current was observed as a function of cathode position. A uniform magnetic field of 30 G was used. The results of these experiments are seen in Table IV. It can be seen that the best performance (discharge efficiency and mass utilization) is obtained when the cathode is nearest the customary location. The magnetic field strength was varied at each cathode location with the usual effect — performance increases with increasing magnetic field up to about 20 G, and then is only slightly affected by further increase in magnetic field strength.

Faraday cup probe measurements of the extracted ion beam profile (radial current density distribution) were made to determine whether cathode locations off-axis created any asymmetry in the extracted ion beam. Some asymmetry was noted in the ion beam profiles; however, it was independent of cathode location and was attributed to nonuniformity in the reverse feed propellant injection tubes.

Keeping the cathode on the discharge axis, the performance was mapped at several distances from the screen. These data are shown in Fig. 17. The best location for the cathode again appears to be farthest from the screen, or nearest the conventional cathode location. It may be noted that the performance seen for this cathode location is somewhat poorer than that for conventional operation of ET I. This results because the variable cathode cannot be put in the "normal" position because of its size and mounting. Further cathode position experiments will be performed with a hollow cathode if operation of this thruster indicates that such experiments would be logical.

TABLE IV

Beam Current (in Milliamperes) as a Function of Cathode Position for Constant Neutral Flow Rate (300 mA Equivalent) and Constant Discharge Power (Z is the Distance of the Cathode from the Screen in cm and R is the Distance of the Cathode from the Discharge Chamber Axis in cm)

Discharge Power Constant at 72 W					
R \ Z	0.3	2.5	4.7	7.3	9.8
0	180	175	185	190	210
1.3	170	185	170	185	205
2.6	155	175	160	165	175
3.8	135	145	130	135	130
5.0	105	75	85	85	75
Discharge Power Constant at 90 W					
R \ Z	0.3	2.5	4.7	7.3	9.8
0	210	215	210	225	240
1.3	205	215	215	215	240
2.6	190	200	205	210	220
3.8	160	165	170	165	165
5.0		110	90		

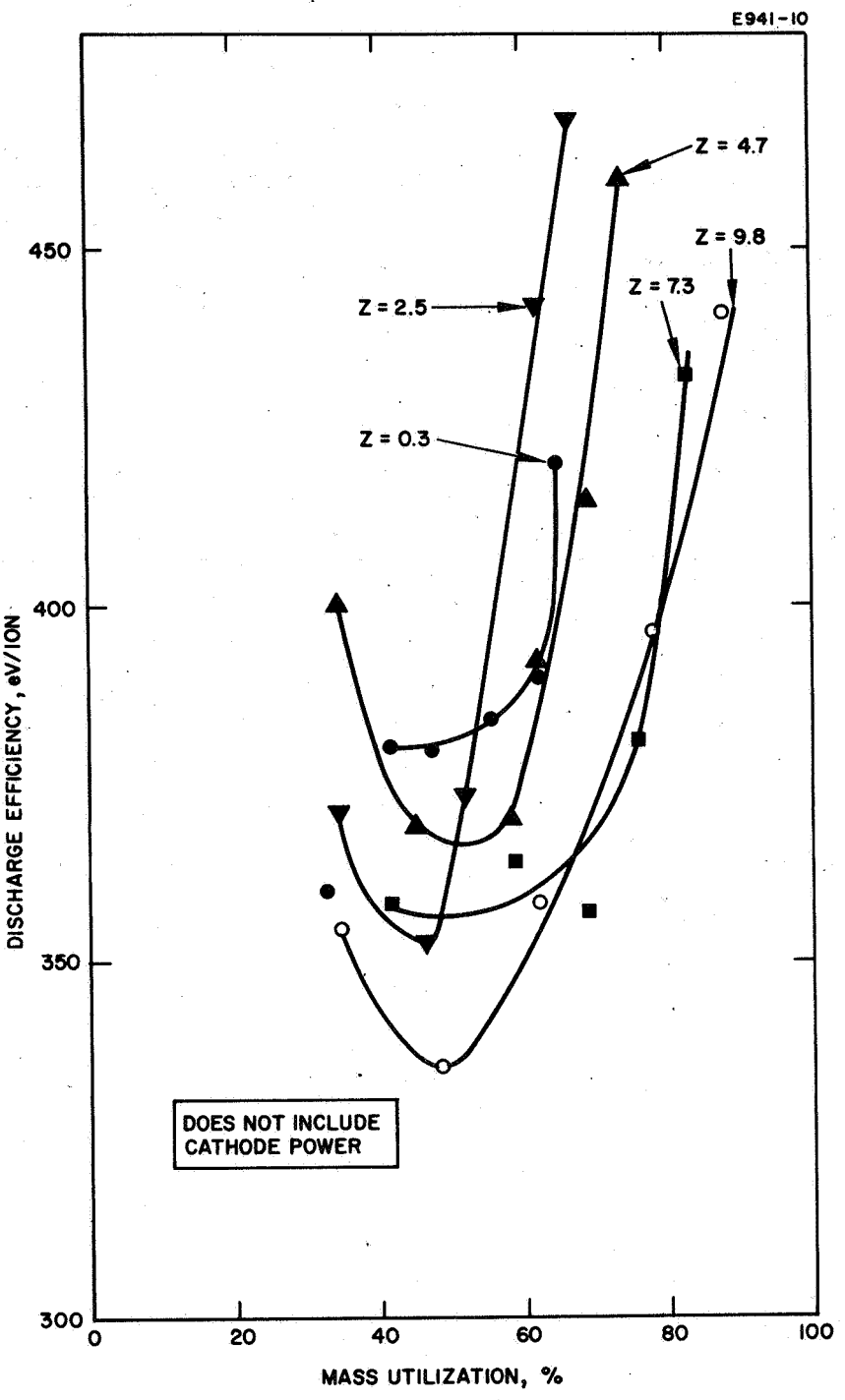

Fig. 17. Performance mapping of discharge efficiency versus mass utilization for variation of cathode position on discharge axis. Z is distance from cathode to screen in centimeters. Thruster parameters are given in Table V.

TABLE V

Thruster Parameters for Performance Mapping with Cathode Position Varied along the Discharge Axis (Shown in Fig. 17)

Z is the distance from cathode to screen
Equivalent neutral flow = 290 mA
Acceleration voltage = 3 kV
Deceleration voltage = 2 kV
Cathode heater voltage = 1.9 V
Cathode heater current = 24.8 A

	Arc Discharge			Ion Beam Performance			
Z, cm	V_D, V	I_D, A	P_D, W	I_{beam}, mA	I_{drain}, mA	η_m, %	eV/Ion
○							
9.8	45	2.5	112	255	1.8	88	441
9.8	38	2.35	90	225	1.8	78	396
9.8	28	2.3	65	180	2.0	62	358
9.8	23.5	2.0	47	140	2.0	48.4	335
9.8	21	1.7	36	100	1.8	34.5	355
□							
7.3	44	2.35	104	240	1.9	82.7	432
7.3	36.5	2.3	82	220	1.9	76	381
7.3	34	2.1	71	200	2.0	69	357
7.3	28	2.2	62	170	2.0	58.6	364
7.3	22	1.95	43	120	2.0	41.5	358
△							
4.7	46	2.2	102	220	2.0	74	460
4.7	41.5	2.0	83	200	2.0	69	415
4.7	32	2.2	70	180	2.0	62	392
4.7	27.5	2.15	59	160	2.0	58.2	370
4.7	23	2.09	48	130	2.0	45	369
4.7	20.5	1.95	40	100	2.0	34.5	400
▽							
2.5	48	1.9	91.2	195	2.0	67	468
	43	1.85	79.5	180	2.0	62	442
	35	1.6	56	150	2.0	52	373
	28	1.7	47.6	135	2.0	46.6	353
	22.5	1.65	37.1	100	1.9	34.5	391
X							
0.3	47	1.7	80	190	2.0	65.5	420
	37	1.9	70.4	180	2.0	62	390
	31.5	1.95	61.4	160	2.0	55.2	384
	28	1.9	53.3	140	2.0	47.2	380
	26	1.75	45.6	120	2.0	41.5	380
	23.5	1.45	34	95	1.8	32.8	360

A hollow cathode was installed in SET II and a baffle shown in the insert of Fig. 18 was mounted on the probe positioning assembly (see Fig. 1) to allow variation in the baffle position. Experiments were performed with the discharge power and neutral flow kept constant and the baffle location varied (along the axis), with uniform and divergent magnetic field configurations. Figure 19 shows the resulting mass utilization as a function of Z, the distance from the baffle to the keep-alive electrode of the hollow cathode. It is apparent that maximum efficiency is achieved when the baffle is closest to the cathode ($z = 0$). The extracted ion beam profile (measured with a Faraday cup probe) is little influenced by the baffle location, as seen in Fig. 19; however, it is somewhat broadened with the divergent magnetic configuration. A performance mapping is shown in Fig. 20 for the baffle located in the optimum position. This is similar in shape to that of the NASA SERT II model thruster, but it displays much lower discharge efficiency (higher eV/ion). It is probable that insufficient neutral pressure is built up in front of the cathode with the simple disc baffle used here. To better confine the neutral flow in the cathode region, the next step will be to enclose the region between the cathode and the baffle with a cylindrical shell, similar in configuration to the cathode pole piece used in the NASA SERT II model thruster. This cylindrical shell will be made of nonmagnetic (stainless steel) material for the first tests and then replaced with a magnetic cylinder identical to that used in the NASA thruster, thus differentiating between the effects of neutral pressure and magnetic shielding of the cathode region. This phase of the research program has just begun, and results are not yet available.

When the hollow cathode was operated as a neutralizer (without a keep-alive electrode) prior to this research contract, rather severe erosion of the cathode face and orifice was observed. Initially, there was some concern about the lifetime of these cathodes for use as a thruster discharge cathode. However, cathode operation at NASA-LeRC produced very little erosion. Comparison of operating procedures disclosed that the only significant difference was the presence of an auxiliary keep-alive electrode in the NASA operation. Since considerable data had been taken to show that the hollow cathode discharge is quite stable without an auxiliary electrode, a set of controlled experiments was performed to determine whether this electrode and the auxiliary discharge could affect the erosion rate. A hollow cathode was operated in a diode configuration (anode located about 2 cm from cathode and biased to collect 0.5 A current) with the keep-alive electrode in position and operating normally, with the keep-alive electrode in position and connected to the cathode, and with the keep-alive electrode removed. Figure 21 shows photographs taken after each of these tests. It is apparent that the keeper electrode plays a role in reducing sputtering erosion of the cathode face and orifice. In the diode tests, the cathode-keeper spacing was 0.070 ± 0.010 in., as specified by NASA-LeRC;

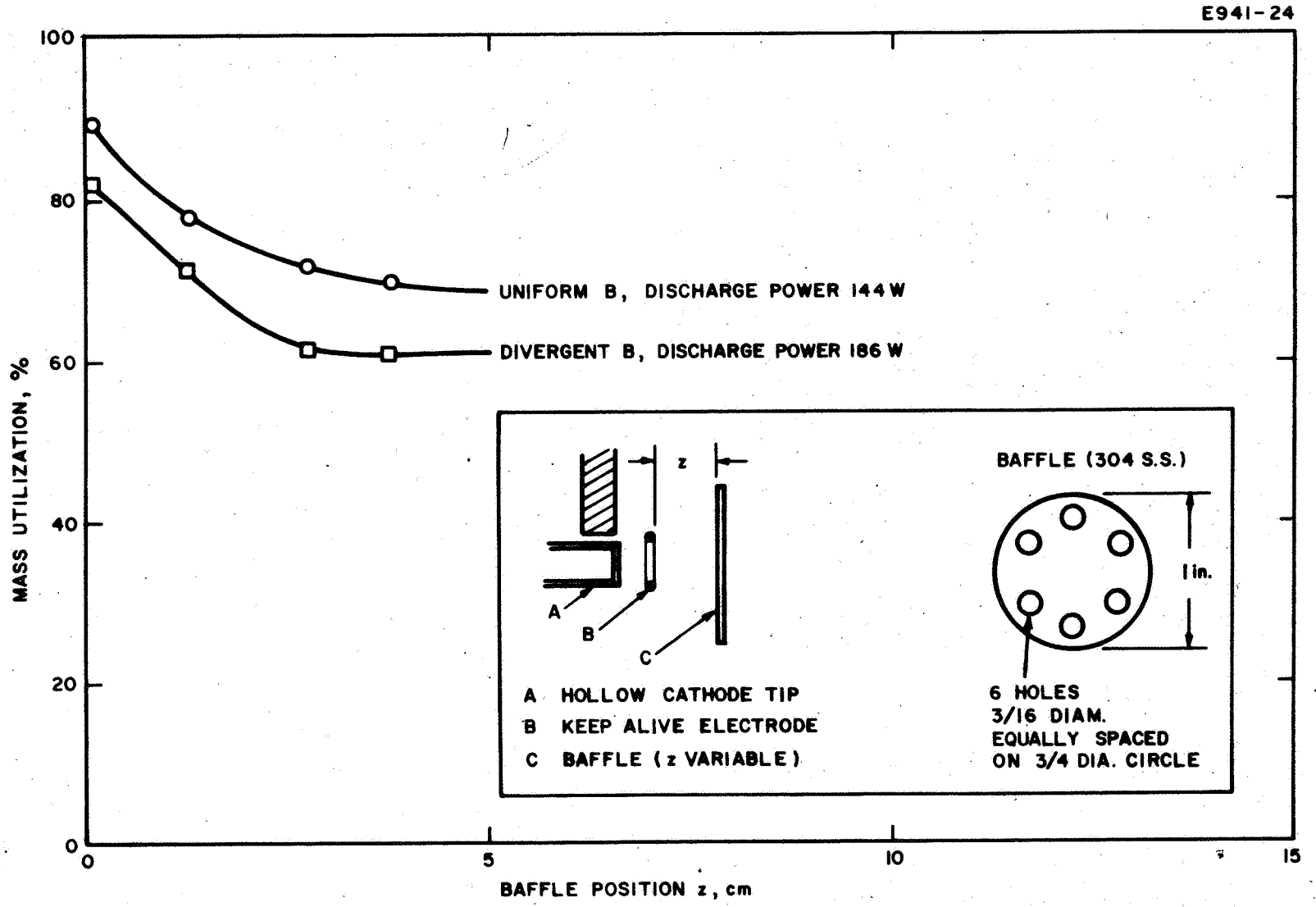

Fig. 18. Mass utilization versus cathode-baffle spacing for ET II operated with a hollow cathode and the baffle shown. Neutral flow and discharge power kept constant.

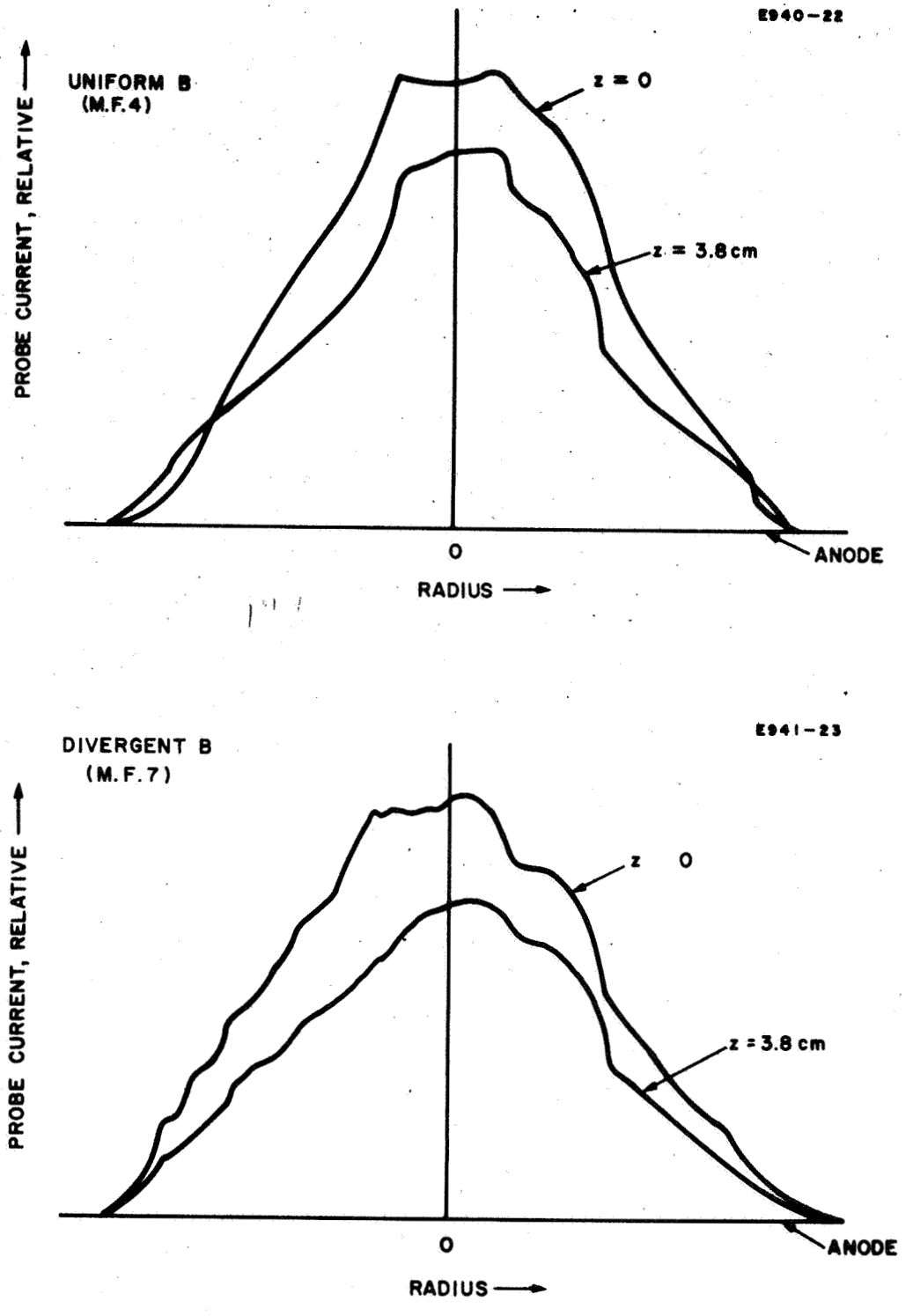

Fig. 19. Ion beam profiles measured with a Faraday cup probe in the beam of ET II. For these profiles, ET II was operated with a hollow cathode (constructed at NASA-LeRC) and the baffle and keep-alive electrode configuration shown in Fig. 18. The parameter Z is the distance from the baffle to the keep-alive electrode. The Faraday cup probe was swept across the beam in a plane 3 cm downstream from the accel electrode.

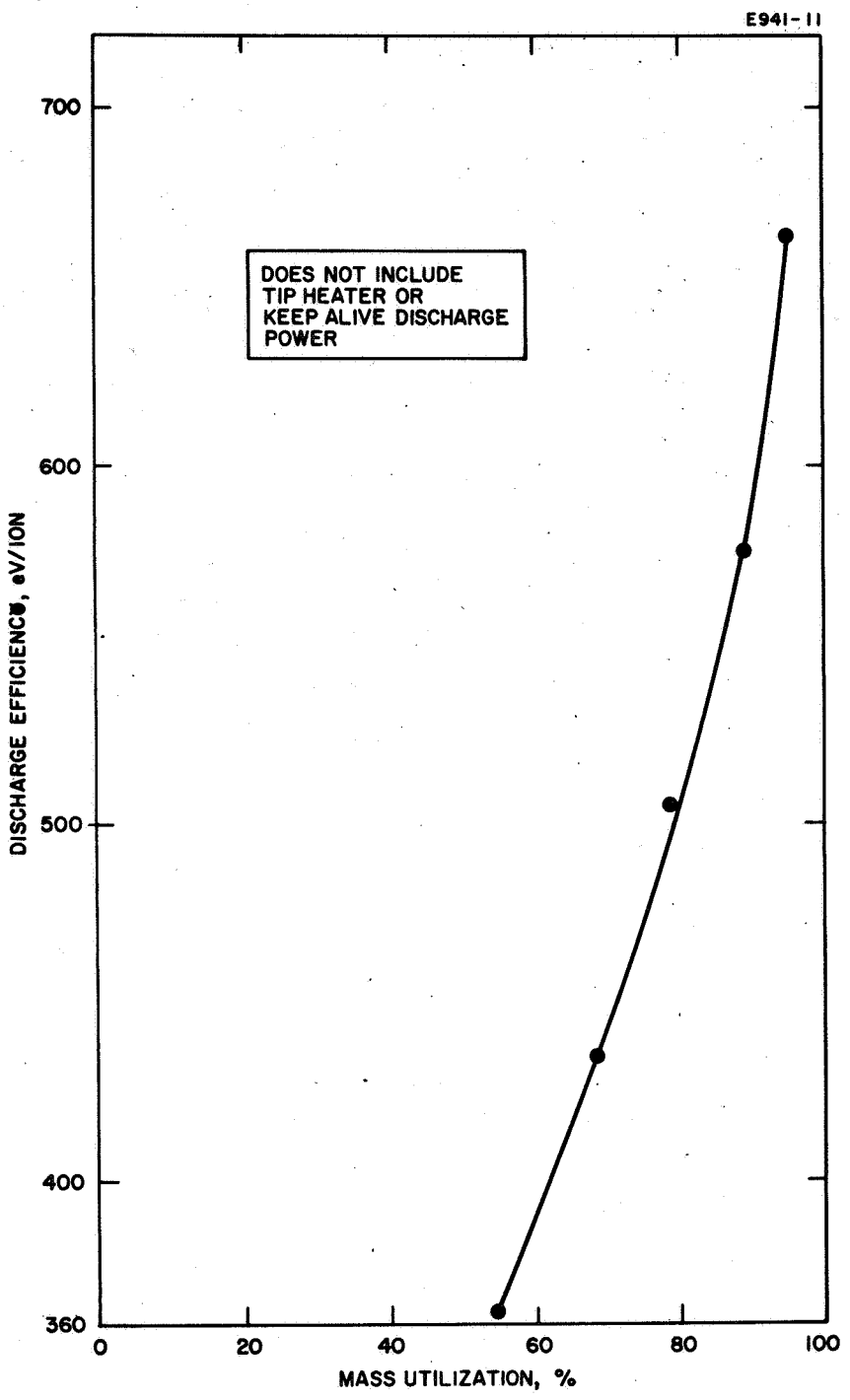

Fig. 20. Performance mapping of ET II operated with a hollow cathode and a simple baffle located in optimum position (thruster data given in Table VI).

TABLE VI

Thruster Parameters for Performance Mapping of ET II Operated with a Hollow Cathode (Fig. 20)

Baffle located as close as possible to keep-alive electrode

Equivalent neutral current through reverse feed system = 268 mA

Equivalent neutral current through hollow cathode = 25 mA

Total neutral current = 293 mA

Acceleration voltage = 3 kV

Deceleration voltage = 2 kV

Arc Discharge			Ion Beam Performance			
V_D, V	I_D, A	P_D, W	I_{drain}, mA	I_{beam}, mA	η_m, %	eV/Ion
31	6	186	6	280	95	664
30	5	150	5	260	88.8	576
29	4	116	4	230	78.5	505
29	3	87	3	200	68.2	435
29	2	58	2	160	54.5	363

Fig. 21. Test of hollow cathode configuration.

(a) New cathode.

(b) Running time 56 hours. Neutral flow 27 ± 5 mA equivalent. Diode characteristics 32 ± 2 V, 0.5 A. Keeper characteristics 10 V, 10 to 50 mA.

(c) Running time 80 hours. Neutral flow 25 ± 1 mA equivalent. Diode characteristics 33 ± 3 V, 0.5 A. Keeper characteristics 0 V, 10 to 100 mA.

(d) Running time 56 hours. Neutral flow 20 ± 1. Diode characteristics 35 ± 1 V, 0.5 A. Keeper removed after starting (large crater on edge is due to contact with keeper when keeper was being removed).

(e) Same cathode as (d) after 10 hours of operation in thruster under a variety of discharge and hollow cathode conditions typically: Discharge conditions 30 V, 2 A. Keeper conditions 10 to 15 V, 0.2 to 0.8 A. Hollow cathode neutral flow 20 to 40 mA equivalent.

Photographs (i) taken perpendicular to cathode face.
Photographs (ii) taken at angle with cathode face.

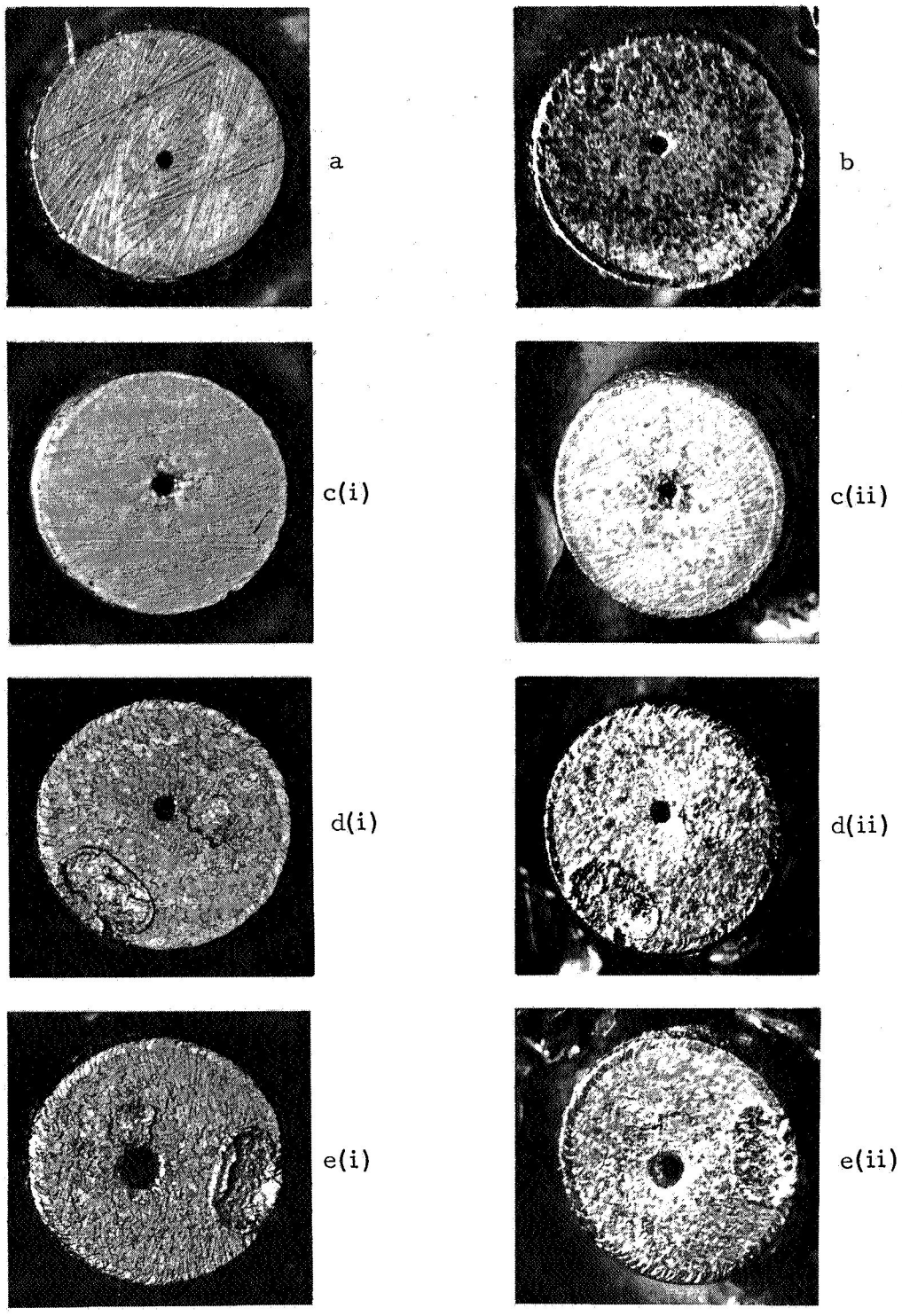

Fig. 21.

however, this spacing could not be maintained accurately in the thruster chamber operation and may have been 0.070 ± 0.025 in., which may account for some of the excess erosion observed. An experiment to probe the plasma region between the keeper and the orifice is in preparation, in order to determine how the keeper discharge modifies the conditions in front of the cathode face. If the presence of the keeper, without the keeper discharge, is sufficient to reduce sputtering and preserve the cathode, the keeper need be turned on only when the cathode is started; this eliminates the need for a specialized power source, and the associated power loss. (Lack of erosion in diode tests does not insure a similar behavior in thruster operation; therefore, similar thruster tests are necessary to justify this conclusion.)

SECTION IV

DISCHARGE THEORY

Work on the discharge theory is still in progress, and only an interim status report can be given. In view of the complicated nature of Penning-type discharges, a valid discharge model cannot be expected solely from first principles. For a realistic approach, guidance must be obtained from observed discharge properties; in addition, the study must be restricted to straightforward discharge geometries. Therefore, all efforts to date were concentrated upon a cylindrical discharge configuration with homogeneous, axial magnetic field and with a thermionic cathode mounted on the axis. Experimental studies of the discharge in this type of geometry (at JPL and at Hughes) have disclosed several characteristic properties from which the following qualitative discharge model may be derived.

Throughout the discharge volume, the plasma potential is above anode potential (by the order of 5 to 10 V), sloping down toward the anode. This suggests that electrons (with a cyclotron diameter on the order of 1 cm) must reach the anode by cross-field diffusion; they cannot rely upon mobility. On the other hand, ions (with cyclotron diameters much greater than the discharge diameter) accelerate toward the anode and reach it in direct ballistic flight.

In typical operation the gas flow rates are on the order of 2×10^{18} atoms/sec in 15 cm discharges, and the ionization efficiencies reach 90%. Under these conditions the gas pressure inside the discharge chamber cannot be much higher than 10^{-5} Torr. At this low pressure, collisions of electrons with neutrals are relatively rare (2×10^{5}/sec at 10^{-5} Torr mercury vapor for 30 eV electrons). In fact, electrons collide more frequently with each other and with ions. In a plasma of 5×10^{11} particles/cm^3, electrons of 30 eV collide with each other at the rate of about 10^{6}/sec. Lower energy electrons collide even more frequently. This high interelectron collision rate makes it plausible that near Maxwellian energy distributions exist among the discharge electrons. While the electrons diffuse outward, they lose energy in exciting and ionizing collisions. Accordingly, their temperature and rate of ionization decrease with radius. Ions generated in the central discharge region accelerate toward the anode under the radial E-field. Upon impact, most of them lose their charge; they rebound as neutrals, but become ionized again in the central region. Eventually, after several "collisions" with the anode, they move sufficiently close to the extraction screen to become drawn out into the ion beam.

Two approaches are being pursued under this contract so that the vague picture described above can be translated into a concrete discharge model. In one case, the discharge is analyzed numerically. All important quantities are evaluated within thin, cylindrical slices of the discharge. The quantities jump discretely from slice to slice, in accordance with physically computed rates of change. This method has led to reasonable profiles of electron density, electron energy, and plasma potential; however, it is not yet sufficiently advanced to be presented in this report. Instead, a second approach will be described in which analytic expressions for the important discharge quantities are being sought. (The actual theoretical treatment appears in the Appendix.) A realistic, relatively uncomplicated formulation of the problem has been achieved. The plasma density distribution can be expressed by a differential equation of the second order. This equation considers the radial growth of the electron current as a result of ionization and the energy losses as a result of ionization and excitation. It assumes that the electron distribution can be described as a Maxwellian at each location. The latter ad hoc assumption is perhaps the weakest point in the theory, and it will be corrected in the future by inclusion of a component of monoenergetic primary electrons.

At present, a computer solution of the differential equation is being sought. Until it is available, a somewhat simplified differential equation, which can be solved analytically, can serve to describe some of the discharge features. The radial plasma density distribution resulting from this solution may be expressed as (see Appendix for the derivation)

$$\rho = \left(2 \frac{j_o r_o}{c_o}\right)^{1/2} (kT)^{1/4} \; B \ln r_1/r$$

where

j_o ≡ radial electron current density at cathode radius r_o

c_o ≡ constant ≅ 1.3

kT ≡ (constant) electron temperature

B ≡ magnetic field

r_1 ≡ anode radius.

Figure 22 shows the resulting radial density distribution. In shape and magnitude the computed distribution closely approaches experimentally observed density profiles (for comparison see Fig. 11), demonstrating the validity of the approach.

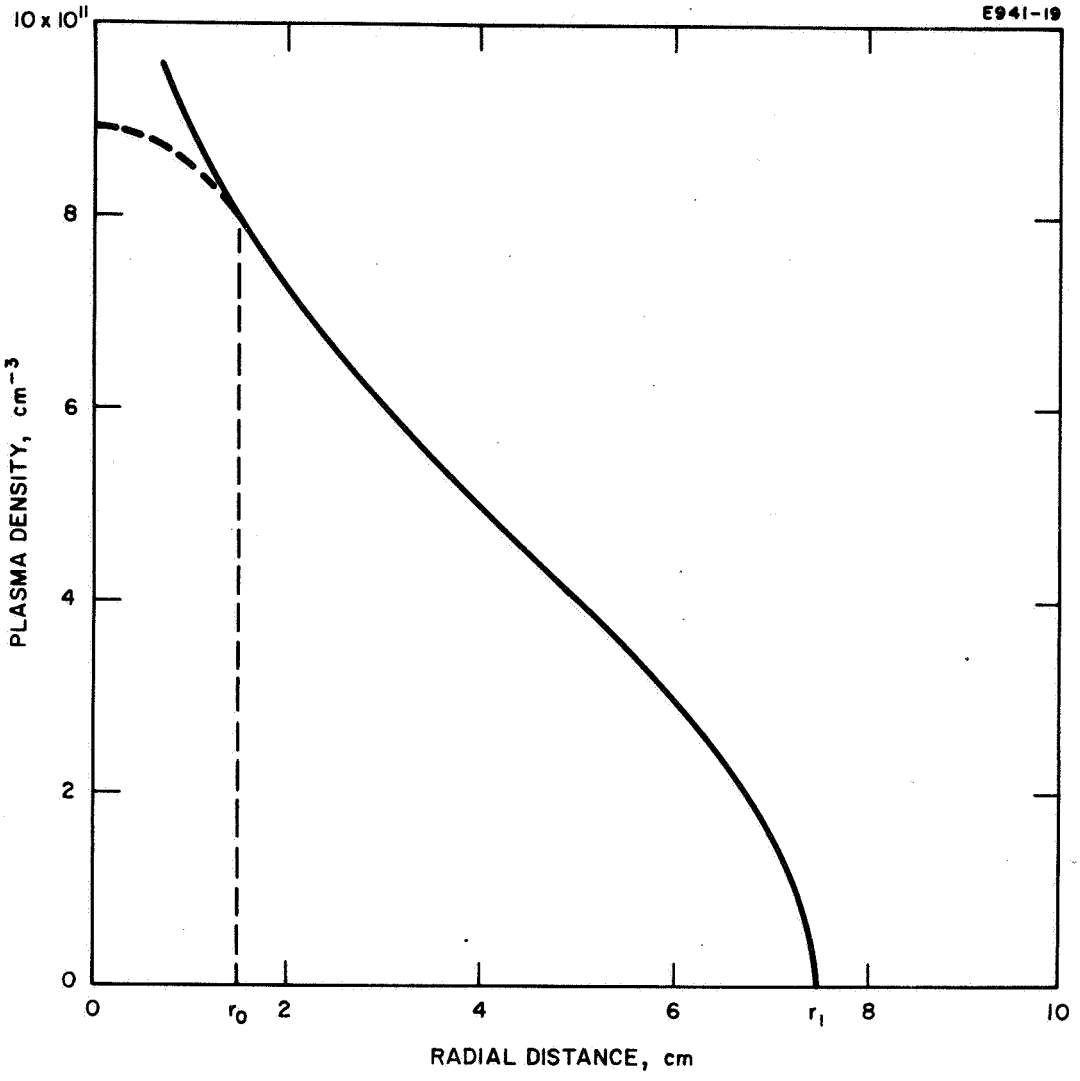

Fig. 22. Radial plasma density distribution according to eq. (19). Discharge current 1.5 A, magnetic field 15 G, electron temperature 6 eV.

SECTION V

SUMMARY

The basic motivation of the present research is to obtain improved thruster performance through improved understanding of the discharge mechanism. Therefore, part of the contract effort is directed toward discharge diagnosis and analysis, and part toward optimization.

Diagnostic and analytic work performed to date has covered

- Magnetic field mappings by iron filings of many B-field configurations of interest, using one of the experimental thrusters built for this program and the NASA thruster
- Langmuir probe measurements of plasma density, plasma potential, and electron energy distribution for different B-field configurations in one of the experimental thrusters
- Measurements of the current density profile of the ion beam as a function of discharge parameters in one of the experimental thrusters
- Analytical studies, forming the basis for a quantitative model of the thruster discharge in a homogeneous magnetic field.

The following results of the diagnostic measurements are perhaps most significant:

1. The plasma density across a discharge with diverging B-field is considerably more uniform than that with a homogeneous B-field
2. The plasma potential has been found to be above anode potential with both homogeneous and diverging B-fields (for oxide cathode operation)
3. The plasma electron "temperature" was determined at some points in the discharge where analysis of Langmuir probe data was possible.

The optimization effort to date has comprised the following tasks:

- Comparative tests of the NASA thruster with magazine, spiral, and hollow cathodes
- Tests of one of the experimental thrusters for various B-field configurations using an oxide cathode
- Tests of one of the experimental thrusters for various cathode positions using an oxide cathode
- Tests of one of the homogeneous B-field thrusters for various baffle configurations using a hollow cathode.

The following significant results have been obtained in the optimization program:

1. At 85% mass utilization, the discharge performance is shown below (lowest eV/ion is best):

Cathode	Spiral Oxide	Magazine Oxide	Hollow
Without Cathode Power	294 eV/ion	415 eV/ion	328 eV/ion
Including Cathode Power	822 eV/ion	1015 eV/ion	525 eV/ion*

2. A strongly divergent field yeilds the best performance (202 eV/ion) at 85% mass utilization.

3. For homogeneous and moderately divergent B-fields the customary cathode position on the axis in the rear is best.

4. A baffle alone is insufficient for good performance. A cylindrical enclosure of the hollow cathode is necessary. (A soft ion enclosure which shields the B-field from the hollow cathode is still under investigation as a nonmagnetic enclosure.)

*Includes keep-alive discharge power.

REFERENCES

1. H. R. Kaufman, NASA TND-585, 1961.
2. W. B. Strickfadden and K. L. Geiler, AIAA J. 1, 1815 (1963).
3. I. Langmuir and H. M. Mott-Smith, Phys. Rev. 735 (1926).

APPENDIX

DISCHARGE THEORY

We assume in our theory that electrons are injected along the discharge axis. Collisions with gas molecules lead to excitations and ionizations, and collisions with ions cause diffusion to the anode. Equations which describe the pertinent electron dynamics include the continuity equation

$$\text{div } j = \bar{\nu}_i \rho \tag{4}$$

where

$j \equiv$ radial electron current density

$\bar{\nu}_i \equiv$ average ionization frequency

$\rho \equiv$ electron density.

An equation of motion is also required to relate the cross-field drift velocity to the driving density gradient $\partial\rho/\partial r$:

$$v_D = -\frac{2}{3}\frac{m}{e^2}\frac{c^2}{B^2}\,(eV)\;\nu_c\,\frac{\partial \rho}{\partial r}\,\frac{1}{\rho}\;(\text{cgs units}) \tag{5}$$

where

$B \equiv$ magnetic field strength

$c \equiv$ velocity of light

$eV \equiv$ electron energy

$\nu_c \equiv$ collision frequency.

Equation (5) applies to an ensemble of monoenergetic electrons. If a distribution of energies exists, the proper averages must be taken. This averaging also must include ν_c which is a function of particle energy for coulomb collisions. If multiple small angle deflections are considered, the coulomb collision frequency can be expressed as

$$\nu_c = 2\pi \ln\Lambda\, e^3 \left(\frac{2}{m}\right)^{1/2} (eV)^{-3/2}\,\rho \tag{6}$$

where $\ln\Lambda$ is a collision parameter (taken to be 15). Introduction of (6) into (5) yields

$$v_D = -40\pi \left(\frac{c}{B}\right)^2 e\,(2m)^{1/2}\,(eV)^{-1/2}\,\frac{\partial\rho}{\partial r} \quad . \qquad (7)$$

Equation (7) will now be averaged under the assumption that the plasma electrons possess a Maxwellian energy distribution at each location. This is considered adequate for an initial approach, particularly since probe measurements point to a large contingent of electrons with near Maxwellian distributions. However, future treatments should include a component of primary electrons with energies corresponding to the acceleration from cathode to anode potential.

In a Maxwellian distribution the number of charges of energy eV is given by

$$d\rho = \left(\frac{4}{\pi}\right)^{1/2} \rho \left(\frac{eV}{kT}\right)^{1/2} \exp\left(-\frac{eV}{kT}\right) d\left(\frac{eV}{kT}\right) \quad . \qquad (8)$$

If (7) and (8) are inserted into

$$\overline{v}_D = \frac{1}{\rho} \int v_D \, d\rho \ ,$$

one obtains

$$\overline{v}_D = -40\,(2\pi m)^{1/2}\, e \left(\frac{c}{B}\right)^2 (kT)^{-1/2}\,\frac{\partial\rho}{\partial r} \qquad (9)$$

or

$$\overline{v}_D = -C_o\, B^{-2}\,(kT)^{-1/2}\,\frac{\partial\rho}{\partial r} \qquad (10)$$

where $C_o \cong 1.3$ cgs units. Equation (10) can be introduced into (4), resulting in the following differential equation for the charge density:

$$\frac{\partial^2\rho}{\partial r^2} + \frac{1}{r}\frac{\partial\rho}{\partial r} + \frac{1}{\rho}\left(\frac{\partial\rho}{\partial r}\right)^2 - \frac{1}{2}(kT)^{-1}\,\frac{\partial(kT)}{\partial r}\,\frac{\partial\rho}{\partial r} + C_o^{-1}(kT)^{1/2}\,B^2\,\overline{\nu}_i = 0 \ . \qquad (11)$$

Since (11) contains two functions of r, a second equation must be provided. The following energy conservation condition can serve this purpose:

$$\frac{d(kT)}{dt} = \frac{\partial(kT)}{\partial t} + v^* \frac{\partial(kT)}{\partial r} \quad . \tag{12}$$

First, since a steady state solution is being sought, the term $\partial/\partial r$ must vanish. Second, the average energy transport velocity v^* is determined by

$$v^* \frac{\partial(kT)}{\partial r} = \frac{1}{\rho} \int v \frac{\partial(kT)}{\partial r} \, d\rho = \frac{1}{\rho} \frac{\partial(kT)}{\partial r} \int v \, d\rho = \bar{v} \frac{\partial(kT)}{\partial r} \; ;$$

therefore, it is identical with the average diffusion velocity $\bar{v}$. Third, the term $d(kT)/dt$ represents the average rate of energy loss by excitation and ionization in a Maxwellian distribution with temperature T. This loss rate and the average ionization frequency $\bar{\nu}_i$ in (11) are functions of the electron temperature

$$\frac{d(kT)}{dt} = - g(kT), \quad \nu_i = k(kT) \; .$$

Both functions can be considered known since they can be derived from available collision data. For example, to obtain $\bar{\nu}_i$ one must take the familiar function of the ionization frequency ν_i versus electron energy eV (see Fig. 23) and compute $\nu_i d\rho$, where $d\rho$ is the number of electrons with energy eV in a Maxwellian distribution of temperature kT (see (8)). Integration over all energies and division by the total charge density

$$\bar{\nu}_i = \frac{1}{\rho} \int \nu_i \, d\rho$$

then yields the average ionization rate at electron temperature T. If this expression is evaluated for a number of different temperatures, the functional dependence $\bar{\nu}_i = k(kT)$ can be found. This dependence has been computed for mercury, (see Fig. 23). It can be seen that over the range of interest of electron temperatures (from about 3 to 20 eV), $\bar{\nu}_i$ increases linearly with T. Accordingly, the following approximation for $\bar{\nu}_i$ will be used here:

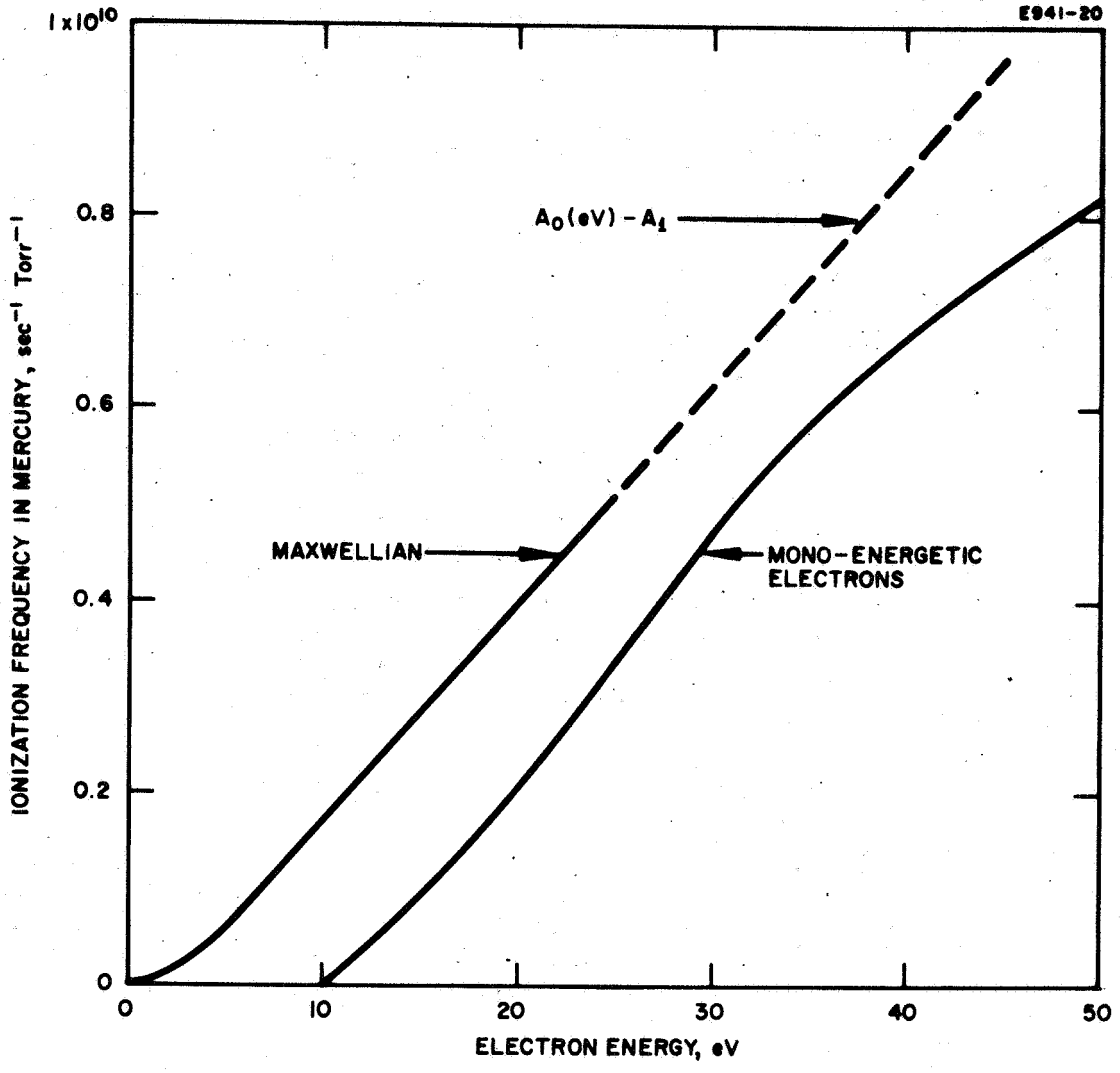

Fig. 23. Ionization rates of monoenergetic and Maxwellian electrons in mercury.

$$\bar{\nu}_i \equiv k(kT) = A_o pkT - A_1 p \qquad (13)$$

where

$$A_o = 1.38 \times 10^{20} \text{ erg}^{-1} \text{ sec}^{-1} \text{ Torr}^{-1}$$

$$A_1 = 6 \times 10^{8} \text{ sec}^{-1} \text{ Torr}^{-1}$$

and p is the gas pressure in Torr.

The average energy loss rate can be determined in a similar fashion from

$$\frac{d(kT)}{dt} = -g(kT) = -(eV_i + kT)\frac{1}{\rho}\int \nu_i \, d\rho - \sum_n eV_{ex}\frac{1}{\rho}\int \nu_{ex} \, d\rho$$

where eV_i is the ionization energy and eV_{ex} is the excitation energy associated with a specific level n. It should be noted that the energy loss in an ionization event also includes the energy which must be supplied to a newly born secondary electron so that it will share the average energy kT.

The energy loss rate $g(kT)$ was determined for mercury, based upon losses associated with ionization (10.38 eV), with excitations involving the transitions $1^1S_1 - 2^3P_2$ and $1^1S_1 - 2^1P$ (4.86 and 6.67 eV), which by far dominate, and including the supply of kT to the newly born electrons. The resultant loss rate curve is shown in Fig. 24. This loss rate function will be approximated by

$$\frac{d(kT)}{dt} \equiv -g(kT) = -A_2 p (kT)^{3/2} \qquad (14)$$

where $A_2 = 1.24 \times 10^{15} \text{ erg}^{-1/2} \text{ sec}^{-1} \text{ Torr}^{-1}$.

Using (10) and (14), the energy conservation relation (eq. (12)) can now be expressed as

$$(kT)^{-2} \, d(kT) = \frac{A_2}{C_o} \, p \, B^2 \left(\frac{\partial \rho}{\partial r}\right)^{-1} dr \qquad (15)$$

or as

$$\frac{1}{kT} - \frac{1}{kT_o} = -\frac{A_2}{C_o} \, p \, B^2 \int \frac{1}{\frac{\partial \rho}{\partial r}} \, dr \; ; \qquad (16)$$

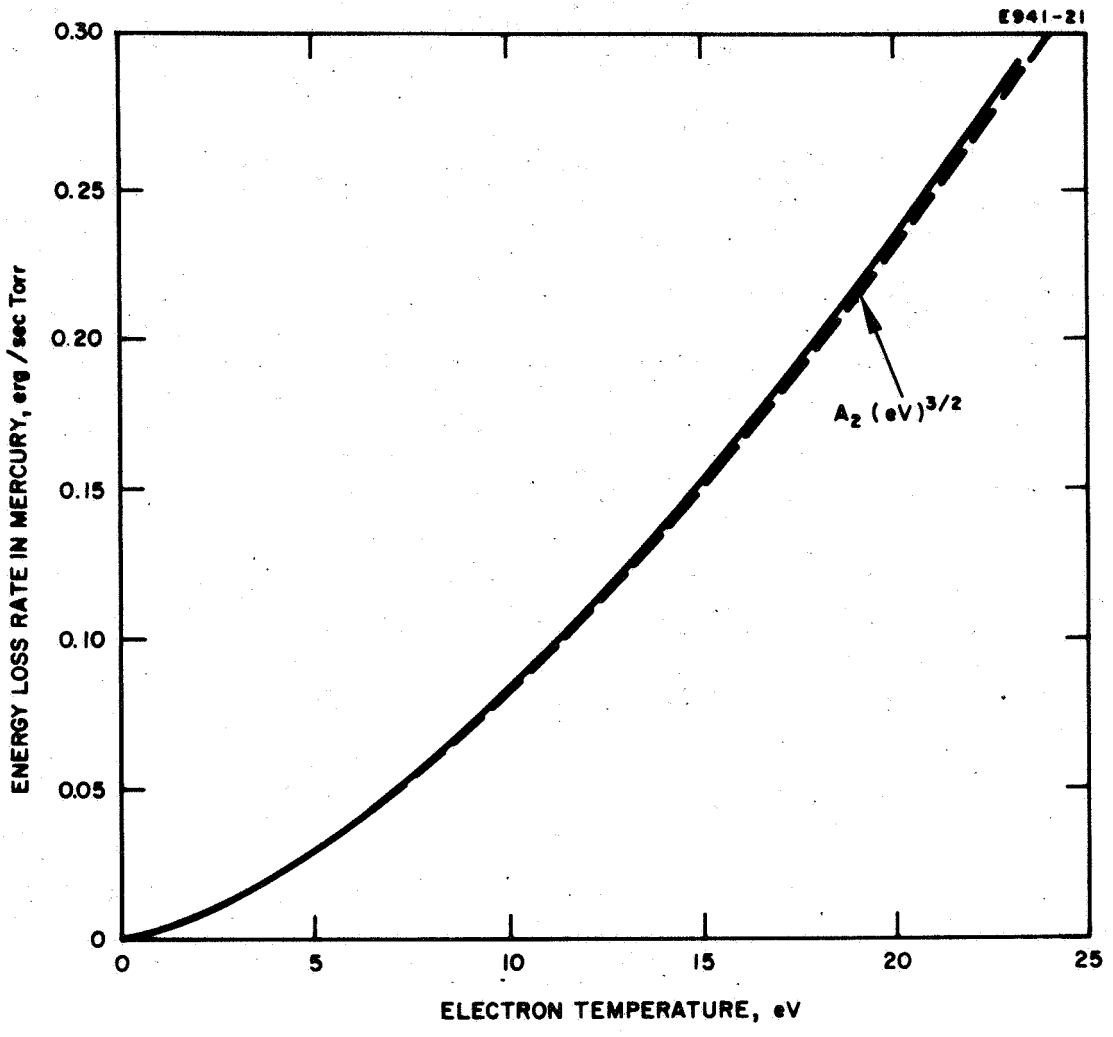

Fig. 24. Energy loss rate of a Maxwellian distribution of electrons as a function of electron temperature in mercury.

or as

$$kT = kT_o \left(1 - \frac{A_2}{C_o}\, p\, B^2\, kT_o \int \frac{1}{\frac{\partial \rho}{\partial r}}\, dr\right)^{-1} \qquad (17)$$

If (13), (15), and (17) are introduced into (11), one obtains

$$\frac{\partial^2 \rho}{\partial r^2} + \frac{1}{r}\,\frac{\partial \rho}{\partial r} + \frac{1}{\rho}\left(\frac{\partial \rho}{\partial r}\right)^2 - \frac{1}{2}\, kT_o \left(1 - C_1\, p\, B^2\, kT_o \int \frac{1}{\frac{\partial \rho}{\partial r}}\, dr\right)^{-1}$$

$$+ C_2\, p\, B^2\, (kT_o)^{3/2} \left(1 - C_1\, p\, B^2\, kT_o \int \frac{1}{\frac{\partial \rho}{\partial r}}\, dr\right)^{-3/2}$$

$$- C_3\, p\, B^2\, (kT_o)^{1/2} \left(1 - C_1\, p\, B^2\, kT_o \int \frac{1}{\frac{\partial \rho}{\partial r}}\, dr\right)^{-1/2} = 0 \qquad (18)$$

where

$$C_1 = A_2/C_o$$

$$C_2 = A_o/C_o$$

$$C_3 = A_1/C_o \ .$$

Solutions to (18) should furnish the density distribution radially across the discharge. With the help of (15) they should also yield the radial electron temperature distribution. Unfortunately, eq. (18) cannot be solved analytically. Therefore, series solutions were attempted. The two series

$$\rho = \rho_o + a_1(r - 1) + a_2(r - 1)^2 + \ldots$$

and

$$\rho = \rho_o + a_1 \frac{r - 1}{r} + a_2 \left(\frac{r - 1}{r}\right)^2 + \ldots$$

were utilized. However, both converged too slowly to give reliable results. A computer solution is now being sought.

Actually, some of the information contained in (18) may be obtained from a simplified differential equation which can be integrated analytically. Assume that the rate of electron generation by ionization and the energy loss by excitation and ionization are both negligible. Equation (18) can be simplified to

$$\frac{\partial^2 \rho}{\partial r^2} + \frac{1}{r}\frac{\partial \rho}{\partial r} + \frac{1}{\rho}\left(\frac{\partial \rho}{\partial r}\right)^2 = 0 \quad . \tag{19}$$

A solution to (19) is

$$\rho = C\ (\ln r_1/r)^{1/2} \tag{20}$$

where $\rho = 0$ for $r = r_1$ (at the anode).

To determine the constant of integration C, one may proceed as follows. With the assumption of a small rate of ionization in (19), the current becomes divergence-free and may be expressed as

$$j \equiv \rho \cdot v_D = j_o\, r_o/r \tag{21}$$

where j_o is the radial current density at the outer cathode radius r_o.

Using (10), (21) may be written as

$$\rho \frac{d\rho}{dr} = - C_o^{-1}\ B^2\ (kT)^{1/2}\ j_o\ r_o/r$$

or integrated

$$\rho^2 = 2\ C_o^{-1}\ B^2\ (kT)^{1/2}\ j_o r_o \ln r_o/r$$

or

$$\rho = \left(2\frac{j_o r_o}{C_o}\right)^{1/2} (kT)^{1/4}\ B \ln r_o/r \quad . \tag{22}$$

The density distribution given by (22) has been evaluated for the following typical discharge parameters:

discharge radius r_1	7.5 cm
cathode radius r_o	1.5 cm
magnetic field B	15 G
electron temperature kT	6 eV (= 2×10^{-2} cgs)
current density j_o at r_o	20 mA/cm^2 (= 6×10^7 cgs)

(total discharge current 1.5 A).

The resulting distribution was shown in Fig. 22. It can be seen that the computed density profile closely resembles profiles obtained by probe measurements in actual thrusters. In addition, the absolute density values appear to be in good agreement with those measured. This is not to say that the simplified solution provided by (19) is fully satisfactory. However, it leads to confidence in future extensions of the chosen model.

Accordingly, future work will be directed toward

(1) completion of a solution for ρ and kT, based on (18)

(2) determination of the radial potential distribution

(3) computation of the ion extraction rates

(4) refinements of the present model through inclusion of primary electrons, through variations across the discharge of the neutral gas density, and through consideration of the finite length of the discharge chamber.